DEVELOPMENT OF XPS DATA ANALYSIS
AND ITS APPLICATION TO
GAS SENSOR AND CATALYST SURFACE STUDIES

Mikko Aronniemi

Laboratory of Physics
Helsinki University of Technology
Espoo, Finland

ABSTRACT OF DOCTORAL DISSERTATION	HELSINKI UNIVERSITY OF TECHNOLOGY P. O. BOX 1000, FI-02015 TKK http://www.tkk.fi

Abstract

In many applications of surface science, the key question is the chemical composition of the surface. X-ray photoelectron spectroscopy (XPS), also known as electron spectroscopy for chemical analysis (ESCA), is an experimental technique which is commonly used in these studies. In this method, the sample is irradiated with x-rays of known energy, thus causing emission of electrons by the photoelectric effect. The binding energy spectrum of these photoelectrons is recorded, and by analyzing the spectrum, the elements and their chemical states can be determined within a few nanometers from the sample surface. The two main steps in the data analysis are subtracting the background intensity caused by inelastically scattered photoelectrons and resolving the overlapping contributions of different chemical species.

This work deals with development of methods for XPS data analysis. Decomposing spectra with overlapping states by curve-fitting is illustrated with a case study of iron and chromium oxides. A lineshape suitable for fitting the core level spectra is described and the differences between three background subtraction methods are investigated. When studying typical sources of uncertainty, the choice of the background turns out to be significant. Factor analysis is presented as an alternative method to determine the contributions of different chemical states in a set of XPS spectra. Aspects affecting the accuracy of the analysis results are pointed out and modifications to a commonly used analysis procedure are proposed. It is shown that in the case of two-component data, a simple scanning of a delta peak along the binding energy axis is capable of generating acceptable component spectra.

The described analysis methods are utilized in two different applications, chromium oxide catalyst and iron oxide gas sensor. In both of these, the functionality of the surface depends strongly on the chemical state of the metal ions. In the catalyst study, XPS is used to analyze the chemical states of chromium in samples subjected to oxidation and reduction treatments. In the case of the gas sensor, XPS provides insight into the sensing mechanism of an iron oxide thin film.

Tekijä	Mikko Aronniemi

Väitöskirjan nimi

XPS-menetelmän data-analyysin kehittäminen ja soveltaminen kaasuantureiden ja katalyyttien pintatutkimukseen

Tiivistelmä

Avainkysymys monissa pintatutkimuksen sovelluksissa on pinnan kemiallinen koostumus. Laajalti käytetty kokeellinen menetelmä tämän selvittämiseen on röntgenherätteinen fotoelekronispektroskopia (XPS, ESCA). Siinä tutkittavaan pintaan kohdistetaan energialtaan tunnettua röntgensäteilyä, joka irrottaa pinnasta elektroneja valosähköisen ilmiön kautta. Näiden ns. fotoelektronien sidosenergiaspektri mitataan, ja spektriä analysoimalla voidaan määrittää alkuaineet ja niiden kemialliset tilat muutaman nanometrin syvyydellä pinnasta. XPS-spektrin analysoinnin pääkohdat ovat epäelastisesti sironneiden fotoelektronien aiheuttaman taustan poistaminen ja spektrissä osittain päällekkäin olevien tilojen intensiteettien määrittäminen.

Väitöskirjassa käsitellään XPS-menetelmän data-analyysin kehittämistä. Spektrissä päällekkäin olevien tilojen erottamista käyränsovituksen avulla havainnollistetaan esimerkillä rauta- ja kromioksideista. Lisäksi esitetään funktio, joka soveltuu hyvin näiden materiaalien sisäkuorten spektrien sovittamiseen, ja tarkastellaan kolmen eri taustavähennysmenetelmän eroja. Tutkittaessa analyysiin liittyviä virhelähteitä taustavähennysmenetelmän valinta osoittautuu merkittäväksi. Toisena menetelmänä kemiallisten tilojen osuuksien selvittämiseen väitöskirjassa tarkastellaan faktorianalyysiä. Työssä käsitellään sen tarkkuuteen vaikuttavia seikkoja ja esitetään muunnos yleisesti käytettyyn analyysitapaan. Lisäksi osoitetaan, että spektrien selittyessä kahdella komponentilla niiden muoto on löydettävissä helposti liikuttelemalla delta-piikkiä sidosenergia-akselilla.

Esitettyjä analyysimenetelmiä sovelletaan väitöskirjassa kahteen tutkimuskohteeseen: kromioksidikatalyyttiin ja rautaoksidikaasuanturiin. Näissä molemmissa pinnan toiminnallisuus riippuu voimakkaasti metalli-ionien kemiallisesta tilasta. Työn katalyyttiä käsittelevässä osassa XPS-menetelmällä analysoidaan kemiallisia tiloja krominäytteestä, joka on altistettu hapetus- ja pelkistyskäsittelyille. Kaasuanturia tutkittaessa XPS-menetelmällä selvitetään rautaoksidiohutkalvon toimintaa kaasuherkkänä materiaalina.

Preface

This thesis has been prepared in the Surface Science Group of the Laboratory of Physics at the Helsinki University of Technology (TKK) during the years 2002–2007. I am grateful to my supervisor Professor Pekka Hautojärvi for giving me the opportunity to work in the Laboratory. I want to thank him also for his encouragement and support; under his supervision I have always been able to trust that my work will lead to dissertation.

I am indebted to my instructor Docent Jouko Lahtinen for his guidance and help. His straightforward attitude to scientific as well as practical issues has helped me get forward numerous times. To Dr. Eeva-Liisa Lakomaa from Vaisala Oyj I wish to express my warmest thanks for interesting discussions and new aspects.

I want to thank the Surface Science Group for creating a pleasant and inspiring working environment. In particular, I am grateful to Dr. Jani Sainio for enjoyable co-operation throughout this work. He has always been willing to help me and his scientific contribution has been crucial on many occasions. The invaluable help of the technical and administrative staff of our Laboratory is greatly appreciated. Very special thanks go to the members of our Lunch Group: Dr. Jukka Katainen, Mr. Matti Paajanen, Dr. Lauri Salminen, and Dr. Jani Sainio. I will remember with warmth our conversations during the lunch and coffee breaks.

The financial support from the Fortum Foundation, the National Graduate School in Materials Physics, and Vaisala Oyj is gratefully acknowledged.

Finally, I would like to thank my parents and parents-in-law for their support and care, my wife Johanna for her love and understanding, and our dear daughters Alma, Elsa, and Helmi for all the joyful color and sound they bring to each day.

Vihti, July 2007

Mikko Aronniemi

Contents

List of publications

This thesis consists of an overview and the following publications:

I M. Aronniemi, J. Sainio, J. Lahtinen, *Chemical state quantification of iron and chromium oxides using XPS: the effect of the background subtraction method*, Surface Science **578**, 108–123 (2005)

II M. Aronniemi, J. Sainio, J. Lahtinen, *Aspects of using the factor analysis for XPS data interpretation*, Surface Science **601**, 479–489 (2007)

III J. Sainio, M. Aronniemi, O. Pakarinen, K. Kauraala, S. Airaksinen, O. Krause, J. Lahtinen, *An XPS study of CrO_x on a thin alumina film and in alumina supported catalysts*, Applied Surface Science **252**, 1076–1083 (2005)

IV M. Aronniemi, J. Lahtinen, P. Hautojärvi, *Characterization of iron oxide thin films*, Surface and Interface Analysis **36**, 1004–1006 (2004)

V M. Aronniemi, J. Sainio, J. Lahtinen, *Characterization and gas-sensing behavior of an iron oxide thin film prepared by atomic layer deposition*, Helsinki University of Technology, Publications in Engineering Physics A, Report TKK-F-A850 (2007)

VI M. Aronniemi, J. Sainio, J. Lahtinen, *XPS study on the correlation between chemical state and oxygen-sensing properties of an iron oxide thin film*, Helsinki University of Technology, Publications in Engineering Physics A, Report TKK-F-A851 (2007). Accepted for publication in Applied Surface Science (2007).

The author has had an active role in all phases of the research reported in this thesis. He has had the main responsibility of the development and implementation of the XPS analysis methods used in publications I–VI. The author has planned the experiments of publications I, II and IV–VI and done most of the measurements of publications IV and V. He has analyzed the XPS data of iron oxides of publications I and II, contributed to the XPS analysis of publication III, and analyzed all data of publications IV–VI. The author has written and is the corresponding author of publications I, II, and IV–VI and has contributed to writing of publication III.

List of abbreviations

AFM	atomic force microscopy
ALD	atomic layer deposition
BE	binding energy
ESCA	electron spectroscopy for chemical analysis
FA	factor analysis
FWHM	full width at half maximum
IC	integrated circuit
IERF	intensity/energy response function
ITTFA	iterative target transformation factor analysis
I–V	current as a function of the voltage
REELS	reflected electron energy loss spectroscopy
SEM	scanning electron microscopy
SNR	signal-to-noise ratio
STM	scanning tunneling microscopy
SVD	singular value decomposition
TFA	target factor analysis
UHV	ultra high vacuum, $\leq 10^{-9}$ mbar
XPS	x-ray photoelectron spectroscopy
XRD	x-ray diffraction

List of symbols

A	state area
	component prediction matrix
B	parameter in the Tougaard background
c_T	constant tail
C	parameter in the Tougaard background
	matrix consisting of coefficients as rows
d	distance between lattice planes
D	data matrix
e_T	exponential slope of a tail
E_0	peak centroid energy
E_b	binding energy
E_k	kinetic energy
E_p	photon energy
f_DS	Doniach–Šunjić function
f_G	Gaussian function
f_GL	Gaussian–Lorentzian product function
f_GLT	Gaussian–Lorentzian product function with a tail
f_L	Lorentzian function
f_T	constant–exponential tail
F	background-corrected photoelectron spectrum
$\hat{F}$	fit to a spectrum
G	recorded photoelectron spectrum
h	peak height
h_T	tail height
K	differential inelastic scattering cross-section
m	set of fitting parameters
M	Gauss–Lorentz mixing ratio
n	integer number
	number of components in the data
n_m	number of free fitting parameters
N	recorded count number
p	number of data points in a spectrum
R	matrix consisting of components as columns
	sensor resistance
s	number of spectra in a data matrix
S	eigenvalue matrix in SVD
T	energy loss in inelastic scattering
	transformation matrix
	temperature

U	eigenvector matrix in SVD
U_B	bias voltage over the sensor
V	covariance matrix
	eigenvector matrix in SVD
x_l	component vector, column of X
X	transformed R matrix
Y	transformed C matrix
α	singularity index of a peak
β	peak half width at half maximum
λ	wavelength
λ_i	inelastic electron mean free path
μ	fitted values for a set of parameters
σ	standard deviation
ϕ	work function
θ	diffraction angle
χ^2	chi-square value of a fit

Chapter 1

Introduction

Surface science is a discipline that deals with interactions between the surface of a solid material and the surrounding environment. Catalysts, gas senors, and various surface treatments are examples of applications in which surface is the functional element. In order to characterize surfaces and understand phenomena taking place on them, several experimental and computational techniques are needed.

In many applications, the key question is the chemical composition of the surface. X-ray photoelectron spectroscopy (XPS), also known as electron spectroscopy for chemical analysis (ESCA), is an experimental technique which is commonly used in these studies. In this method, the sample is irradiated with x-rays of known energy, thus causing emission of electrons by the photoelectric effect. The binding energy spectrum of these photoelectrons is recorded, and by analyzing the spectrum, the elements present within a few nanometers from the sample surface can be identified and their relative abundances can be determined. Moreover, in many cases also the different chemical states of the elements can be distinguished.

The physical basis of XPS, the photoelectric effect, was discovered by Hertz in 1887 and explained by Einstein in 1905. The first XPS setups were constructed for studies of electronic structure of atoms in the beginning of the 20th century. The usefulness of XPS for chemical analysis of surfaces was discovered in the 1950s, especially due to the work of Siegbahn [1] leading to significantly higher spectrometer resolution. Commercial XPS instruments have been available since 1969 and today XPS is an important tool for surface scientists around the world. Einstein was awarded the Nobel Prize in 1921 for his discovery of the law of the photoelectric effect and Siegbahn in 1981 for his contribution to the development of high-resolution electron spectroscopy [2].

Characteristic of XPS is that the complexity of the analysis procedure depends

strongly on the properties of the sample and, in particular, on the desired accuracy of the sought chemical information. For example, a routine identification of elements and their abundances in a flat, homogeneous, and conductive sample is typically straightforward. On the contrary, the analysis may be very demanding for a rough, inhomogeneous, and insulating sample, especially if the amounts of the elements and their chemical states need to be determined accurately. In such a case, a reliable analysis requires detailed knowledge on the physics behind the photoelectron spectrum, careful structural characterization of the surface, and sophisticated mathematical methods for the data analysis.

This work contributes to the development of quantitative XPS analysis, in particular the quantification of chemical states of transition metal oxides in the case of homogeneous in-depth distribution. The materials studied here are oxides of iron and chromium in various forms of samples. These materials have industrial applications, for example, in catalysis, gas detection, steel fabrication, pigments, and magnetic storage media. In this work, Publications I and II deal with the XPS data analysis and Publications III–VI are concerned with the use of XPS, along with other surface analysis techniques, in catalyst and gas sensor studies. Publication I presents a case study of iron oxide and chromium oxide samples and focuses on the two major steps in the XPS data analysis: background subtraction and separating contributions of overlapping chemical states by curve-fitting. Publication II describes the use of factor analysis in quantification of chemical states in XPS data. Factor analysis is a multivariate statistical method which may allow a convenient analysis of a series of XPS spectra; interestingly, factor analysis provides a fundamentally different means to XPS analysis compared with the curve-fitting addressed in Publication I. Publication III illustrates the use of XPS in catalyst studies. The objective there is to compare the behavior of a chromium oxide model catalyst to two industrial catalysts. Regarding the properties of a chromium oxide catalyst, the analysis of the chemical states is particularly important because only one of the five possible chemical states, namely Cr^{3+}, is proposed to be catalytically active. Publications IV–VI deal with the use of an iron oxide thin film as a gas sensitive material. The effect of growth parameters on the film properties are considered in Publication IV, the film characteristics and gas-sensing properties in Publication V, and finally the correlation between the chemical state and sensing behavior in Publication VI. In this application, too, one of the most critical material properties is the chemical state of the active metal species on the surface.

Chapter 2

Experimental

2.1 X-ray photoelectron spectroscopy (XPS)

In XPS, the sample surface is irradiated with x-rays. If the interaction between an x-ray photon, having energy E_p, and an electron of an atom in the sample leads to photoionization, the electron leaves its parent atom and becomes a photoelectron with kinetic energy

$$E_k = E_p - E_b - \phi \qquad (2.1)$$

where E_b is the binding energy of the electron with respect to the Fermi level and ϕ is the work function. Some of the photoelectrons are able to escape from the sample, and by measuring their kinetic energy, a binding energy spectrum of the photoelectrons is obtained through the equation above. The x-ray energy E_p is determined by the anode material; the most common are aluminum and magnesium whose K_α energies are 1486.6 eV and 1253.6 eV, respectively. The exact value of the work function is usually unknown so the energy scale of the spectrum has to be calibrated using a known reference.

A binding energy spectrum can be used to identify the elements in the sample. Each element has a unique electronic structure and peaks are observed in the spectrum at energies corresponding to the energy levels. The peaks are commonly denoted as nl_j where n is the principal quantum number, l is the orbital quantum number (as a letter: s=0, p=1, d=2,...), and $j = |l + s|$ is the total angular momentum including the spin quantum number $s = \pm 1/2$. The relative amounts of the elements in the sample can be determined by comparing the intensities of the corresponding peaks. Here, however, factors affecting the sensitivity of the elements in XPS, such as photoionization cross section, inelastic mean free path, and elastic scattering properties, have to be taken into account. The area of a given peak is also strongly affected by the in-depth distribution

of the corresponding element: the longer the photoelectrons travel within the sample, the larger is the fraction that loses energy and thereby contributes to the inelastic background instead of the elastic peak. Thus, for reliable chemical quantification, knowledge on the surface structure is essential. If the structure cannot be assumed homogeneous, information on it can be obtained by analyzing the inelastic background of the peaks, by varying the angle of the sample surface (angle-resolved XPS), or by depth profiling (sputtering the sample with noble gas ions).

Although each energy level of an isolated atom has a characteristic binding energy, the kinetic energies of photoelectrons originating from a given energy level are not exactly equal when they leave the sample surface. Thus, broadening, asymmetry, and shifting of the peaks are observed in the recorded spectrum. The processes that affect the energy of a photoelectron can be classified in three groups: initial state effects, final state effects, and extrinsic losses. *Initial state effects* influence the binding energy (E_b in Eq. (2.1)) of a given level before the photoionization process. These effects include chemical shifts due to, e.g., bonding and oxidation/reduction. In fact, it is just the ability to resolve these chemical shifts which makes XPS a valuable tool in chemical analysis. For example, the $2p_{3/2}$ peak of the Fe^{2+} state is shifted by 2.7 eV and the Fe^{3+} state by 4.2 eV from the metallic state; both of these can be easily distinguished with a typical XPS system. *Final state effects* take place during the photoionization process. They are caused by the relaxation of the electrons of the atom in response to creation of the hole. As a result, the parent atom is left in an excited state and the photoelectron is emitted with a lower kinetic energy E_k. The final state effects are in many cases characteristic for some chemical state and can thereby be used as fingerprints when identifying the states. For example, the Fe^{2+} state has a satellite peak 6 eV below the main $2p_{3/2}$ peak whereas this separation is 8 eV for the Fe^{3+} state. The final state effects are commonly referred to as intrinsic losses, indicating that they take place within the parent atom. *Extrinsic losses*, on the contrary, are processes that reduce the kinetic energy of a photoelectron after it has left the parent atom. These effects include inelastic scattering from other electrons within the sample and interaction with plasmons. The extrinsic losses produce a wide, even hundreds of eVs, background which usually needs to be subtracted before determining the peak intensities. By analyzing the shape of the background, information on the in-depth distribution of the elements can be obtained. Generally, the higher the background, the deeper the element is located. In addition to the processes affecting the binding or kinetic energy of a photoelectron, broadening or shifting of the peaks may be caused by variations in the work function ϕ. This is commonly observed in the case of insulating samples which tend to charge non-uniformly as a result of the photoelectron emission.

High surface-sensitivity, i.e. short information depth, of XPS results from the

high interaction probability of photoelectrons within the sample. Only the photoelectrons generated within a few nanometers from the surface may reach the surface without losing their energy in inelastic scattering. The lateral resolution of XPS is mainly determined by the x-ray spot size. Typical values are between 10 μm and 1 mm.

An XPS instrument includes an electron gun and anode for generating x-rays, an energy analyzer and detector to record the spectrum, control electronics, and a computer for control and data acquisition. The sample and a part of the instrumentation are mounted in a vacuum chamber to reduce contamination of the surface and to minimize collisions of the ejected photoelectrons with gas molecules.

2.2   Other techniques used in this work

Although sensitive to the chemical environment of an atom, XPS is typically unable to distinguish between two structures which have the same chemical composition but different ordering of the atoms. For example, iron oxide has α-Fe$_2$O$_3$ and γ-Fe$_2$O$_3$ phases, both of which have iron atoms only in the Fe^{3+} state and cannot thus be distinguished with XPS. X-ray diffraction (XRD) is a method which is sensitive to the crystal structure of a sample. It is based on Bragg's law of diffraction which states that when a sample is irradiated with monoenergetic radiation, intensity maxima are observed in angles θ given by

$$\sin \theta = \frac{n\lambda}{2d} \tag{2.2}$$

where n is an integer, λ is the wavelength of the x-rays, and d is the distance between lattice planes. In practice, the intensity of diffracted x-rays is recorded as a function of the angle, and the angles giving the intensity maxima are compared with a database containing the diffraction patterns of several structures. It is to be noted, however, that XRD cannot detect amorphous materials.

In order to study the topographical structure of a sample, such as the grain size, atomic force microscopy (AFM) and scanning electron microscopy (SEM) are commonly used. In AFM, measuring the distance between a sharp tip and the sample surface is based on the short-range electrostatic forces, such as van der Waals and dipole–dipole forces. The tip, placed in the end of a cantilever, is brought close to the surface and the bending of the cantilever is measured using a laser and photodiode. In this work, the images were recorded in the dynamic mode in which the cantilever is made to oscillate close to its resonant frequency and the distance between the tip and the surface is obtained from the modulation of the amplitude. In SEM, an electron beam with a spot size of a few nanometers,

is scanned over the sample. The image is constructed so that the intensity of a given pixel is determined by the intensity of detected secondary and/or backscattered electrons corresponding to that point on the surface. Compared to AFM, imaging with SEM is faster and easier but the lateral resolution is typically lower; in addition, SEM produces no direct height information of the surface structures and is sometimes difficult to use with insulating samples.

Chapter 3

XPS data analysis

Reliable quantification of elements and their chemical state requires a detailed analysis of the photoelectron spectrum and some information on the surface structure. The two main steps in the analysis are subtracting the background intensity caused by inelastically scattered photoelectrons and resolving the overlapping contributions of different chemical species. In addition, due to the high surface-sensitivity of XPS, the in-depth distribution of the analyzed species needs to be considered carefully. On one hand, the intensity of the elastic peak is strongly affected by the excitation depth of the photoelectrons. On the other hand, the shape of the inelastic background may provide information on the surface structure.

The main use of XPS in this work was quantification of the chemical states of iron and chromium oxides. The samples were bulk-like powders and thin films, so the in-depth distribution of the chemical states could be assumed homogeneous. In this chapter, the different background subtraction methods and details of curve-fitting are first considered in a case study of iron and chromium oxides (Publication I). Then, the use of factor analysis as an alternative method to decompose the chemical states is illustrated (Publication II). For factor analysis, aspects affecting the accuracy of the results are also pointed out and modifications to a commonly used analysis procedure are proposed.

3.1   Background subtraction

The *Shirley background* [3] is the conventional way to remove the contribution of inelastic photoelectrons. It is subtracted from the recorded spectrum G iteratively

as

$$F_{n+1}(E_\mathrm{k}) = G(E_\mathrm{k}) - G(E_\mathrm{k,min}) \frac{\int_{E_\mathrm{k}}^{E_\mathrm{k,max}} F_n(E_\mathrm{k}') \, \mathrm{d}E_\mathrm{k}'}{\int_{E_\mathrm{k,min}}^{E_\mathrm{k,max}} F_n(E_\mathrm{k}') \, \mathrm{d}E_\mathrm{k}'} \qquad (3.1)$$

where F_n is the background-corrected spectrum after n iterations. The series converges typically after a few iterations and then the background intensity at a given energy is directly proportional to the background-subtracted intensity at the high kinetic energy side. For the Shirley background, the only parameters needed are the endpoints of the range over which it is calculated, i.e. $E_\mathrm{k,min}$ and $E_\mathrm{k,max}$. Although producing reasonable spectra in many cases, the Shirley background is empirical in nature.

The *Tougaard background* is based on rigorous modeling of the inelastic scattering of electrons within a solid [4]. According to it, the background correction for a homogeneous and infinite depth distribution (i.e. bulk sample) is calculated as

$$F(E_\mathrm{k}) = G(E_\mathrm{k}) - \lambda_\mathrm{i} \int_{E_\mathrm{k}}^{\infty} G(E_\mathrm{k}') \; K(E_\mathrm{k}' - E_\mathrm{k}) \; \mathrm{d}E_\mathrm{k}' \qquad (3.2)$$

where λ_i is the inelastic electron mean free path and $K(E_\mathrm{k}' - E_\mathrm{k})$ is the differential inelastic scattering cross-section [4]. The cross-section can be determined experimentally for the studied sample but Tougaard et al. have shown that for most metals, their oxides and alloys, the product of the inelastic mean free path and the inelastic scattering cross-section is only weakly dependent on E_k and can be approximated with a so-called universal formula

$$\lambda_\mathrm{i} \; K(T) = \frac{BT}{(C + T^2)^2} \qquad (3.3)$$

where T is the energy loss in eV and B and C are parameters [4–6]. When constructing the background function, B is a fitting parameter which is adjusted so that $F(E)$ goes to zero in a wide energy range about 30–50 eV below the peak. By fitting function (3.3) to the calculated dielectric response data, Tougaard has obtained values $B \approx 3000 \; (\mathrm{eV})^2$ and $C = 1643 \; (\mathrm{eV})^2$ for homogeneous bulk samples. Although Eq. (3.2) was derived assuming homogeneous and infinite depth distribution, it can be used for a wide range of depth profiles with reasonable accuracy by scaling B [7]. However, for materials with a distinctive plasmon structure, a three-parameter universal cross-section should be used instead of Eq. (3.3) [8].

Compared to the calculated dielectric response data, a more direct way to determine the electron transport properties is to use reflected energy loss spectroscopy (REELS) [8–10]. *Seah* has proposed a modified method to determine the values of B and C parameters in which C becomes element-specific and B can again

be adjusted in fitting [11]. Based on REELS measurements of 59 elements, Seah et al. have derived a new set of parameters which can be used in Tougaard's formalism for constructing an element-specific inelastic background [9, 11]. For example, the values of C for iron and chromium are 756 $(\text{eV})^2$ and 806 $(\text{eV})^2$, respectively [9].
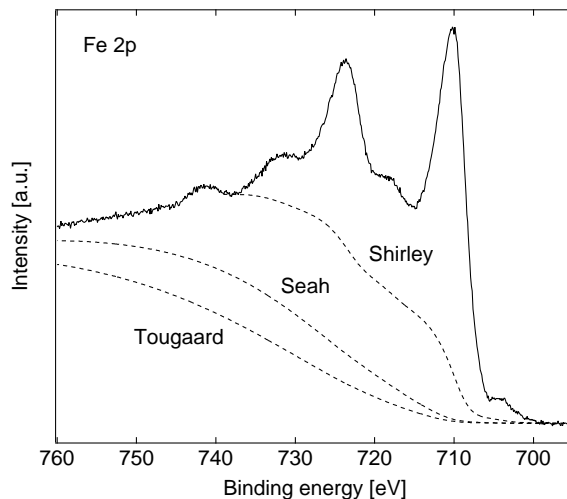

Figure 3.1: *Examples of the Shirley background, the universal Tougaard background, and Seah's modification of the Tougaard background. The spectrum is the Fe 2p region recorded from an iron oxide powder sample.*

Figure 3.1 shows examples of the three background subtraction methods applied to an Fe 2p spectrum. The advantage of using a Tougaard-type background is that the background at a given energy is calculated using the measured spectrum at higher kinetic energies and is therefore independent of the endpoint selection as long as the spectrum is wide enough so that the correct value for B can be determined. It should be noted that a Tougaard background can also be calculated for a shorter spectrum if the values of B and C have been determined earlier using a wider range spectrum or can be estimated. Végh has pointed out that also the Shirley background can be expressed in the Tougaard formalism by choosing an appropriate $\lambda_i K(T)$ function [12]. This facilitates the comparison between these two background models.

The Tougaard method has previously been compared to the Shirley and linear backgrounds in Ref. [13]. In that work, the peak intensities of polycrystalline elemental solids were compared with the theoretical values and the compositions of binary alloys were determined; in addition, the consistency of the results was studied. In Ref. [14], the consistency and validity of these three background

subtraction methods were studied as an interlaboratory comparison. In both of these studies, the performance of the Tougaard method was found to be the best. Thus, it could be stated that a Tougaard-type background should be used also in the chemical state quantification if a compatible lineshape can be determined.

If the energy range to be analyzed is wide, the recorded spectrum should be corrected for the energy-dependent efficiency of the analyzer before the background subtraction. The intensity/energy response function (IERF) for this purpose can be obtained through a calibration procedure. For the equipment used in this work, however, the exact IERF was not available but an approximate formula was used

$$G(E_k) = G_0(E_k) \cdot E_k^{0.7} \tag{3.4}$$

where G_0 is the original recorded spectrum. The exponent value of 0.7 was provided by the manufacturer [15].

3.2 Curve-fitting

Curve-fitting is a common way to separate the contributions of overlapping chemical states in a photoelectron spectrum. When using this approach, the analyst chooses a mathematical function to describe the spectrum of each state and fits these functions to the data. Typically, some knowledge on the parameters of the functions, such as the position of the intensity maximum, can be utilized in the fitting. One of the objectives of this work was to find an analytical lineshape which can reproduce the 2p spectra of the Fe^{2+}, Fe^{3+}, Cr^{3+}, and Cr^{6+} states, and which can be used as a convenient fitting function in a curve-fitting algorithm. Such a representation allows also replacing the experimental data with a set of parameters that can be transferred and compared with other studies.

Lineshapes

After the photoemission the atom is left with a core hole that has a finite lifetime. This makes the lineshape of the photoelectron peak corresponding to a given energy state inherently Lorentzian [16]

$$f_L(E_b) = h \left[1 + \left(\frac{E_0 - E_b}{\beta} \right)^2 \right]^{-1} \tag{3.5}$$

where E_0 is the centroid energy, h is the height, and β is the half width at half maximum.

In practice, the peaks are broadened due to the energy distribution of the x-ray photons, various interactions of the photoelectrons, e.g. with phonons, and the finite spectrometer resolution. These effects can be taken into account by convoluting the intrinsic lineshape with a Gaussian [17]

$$f_{\mathrm{G}}(E_{\mathrm{b}}) = h \ \exp\left[-\ln(2)\left(\frac{E_0 - E_{\mathrm{b}}}{\beta}\right)^2\right].\qquad(3.6)$$

The convolution of a Lorentzian with a Gaussian is called a Voigt lineshape.

As mentioned above, the energy of a photoelectron may be influenced by several final state effects. In the case of metals, there is a continuous distribution of final states which are caused by the core hole interaction with valence band electrons. As a result, the metallic core level peaks have a long, asymmetric tail. The core level peaks of metal oxide states are wider and have shorter tails. A prominent difference is also the presence of discrete satellite peaks. They are caused by the configuration interaction due to relaxation of the valence electrons, which involves also significant ligand–metal charge transfer [18]. Another characteristic feature of the oxide states is the multiplet splitting. For the 2p states, it is caused by the interaction between the 2p electrons and the unpaired 3d electrons, and it results in a multitude of possible final states [19]. For most of these states, however, the energy separation is so small that no discrete peaks will appear with a typical spectrometer resolution. Consequently, the multiplet splitting is seen in the spectrum as asymmetric broadening of the peaks.

Due to the various final state effects, an asymmetric lineshape may be necessary to represent the core level peaks in a photoelectron spectrum. For metallic states, the Doniach–Šunjić (D–S) function is commonly used

$$f_{\mathrm{DS}}(E_{\mathrm{b}}) = h \ \frac{\beta\cos\left[\frac{\pi\alpha}{2} + (1-\alpha)\arctan(E_0/\beta)\right]}{[(E_0 - E_{\mathrm{b}})^2 + \beta^2]^{(1-\alpha)/2}}\qquad(3.7)$$

where E_0, h and β are as above, and α (≥ 0) is the singularity index describing the asymmetry of the peak [20]. If α is set to zero, this lineshape is reduced to a symmetric Lorentzian (Eq. (3.5)). It should be noted that in the case of asymmetric peak, i.e. $\alpha > 0$, parameters h, E_0, and β are not the exact height, location, and width of the peak, respectively, but can be used to describe them. However, a convolution of the D–S lineshape and a Gaussian broadening function cannot be written in a closed form, which makes the fitting computationally heavy. For this reason, approximative representations are commonly used as a fitting function instead of the true convolution. In this work, a Gaussian–

Lorentzian product function f_{GL} with a constant–exponential tail f_T was used [17]

$$f_{GL}(E_b) \;=\; \left\{ \left[1 + M\frac{(E_0 - E_b)^2}{\beta^2}\right] \exp\left[(1-M)\frac{(\ln 2)(E_0 - E_b)^2}{\beta^2}\right] \right\}^{-1} \quad (3.8)$$

$$f_T(E_b) \;=\; c_T + h_T\,\exp\left[-(E_b - E_0)\frac{e_T}{\beta}\right] \quad (3.9)$$

where M is the Gauss–Lorentz mixing ratio ranging from 0 for a pure Gaussian to 1 for a pure Lorentzian peak, c_T determines the height of the constant part of the tail, h_T is the height and e_T is the slope of the exponential part of the tail. The tail is combined with the peak at the high binding energy side to form the total function f_{GLT}:

$$f_{GLT}(E_b) \begin{cases} = h\,\{f_{GL}(E_b) + [1 - f_{GL}(E_b)]\,T\} & \text{for } E_b > E_0 \\ = h\,f_{GL}(E_b) & \text{for } E_b \le E_0 \\ \ge 0 & \text{for all } E_b. \end{cases} \quad (3.10)$$

This lineshape was found to be well suited to represent, besides the metallic states, the 2p peaks of iron and chromium oxides subject to strong multiplet splitting, as long as the instrumental broadening makes the multiplet states unresolved. A representation for a complete 2p region of a given chemical state was obtained by summing a necessary amount, typically four, of these peaks. For the satellite peaks, though, no tail was needed.

Uncertainty in curve-fitting

Figure 3.2 shows an example of chemical state quantification based on curve-fitting with the lineshape described above by Eq. (3.10). It also illustrates the differences between the three background subtraction methods presented above in Sect. 3.1. When analyzing the data, the lineshape was first fitted to a reference spectrum (Fig. 3.2a) recorded from a sample which could be assumed to contain only the Fe^{3+} state. The small peak observed at about 704 eV was ascribed to In $3p_{1/2}$ from the indium foil and was not included in the analysis. Then, the spectrum to be analyzed (Fig. 3.2b) was fitted with two states corresponding to Fe^{2+} and Fe^{3+}. In the fitting process, the parameters of the Fe^{3+} state were fixed to the values obtained from the reference spectrum and the binding energy separation between the Fe^{2+} and Fe^{3+} states was fixed to 1.4 eV.

The correspondence between the recorded data F and the fit $\hat{F}$ can be described with a reduced chi-square value defined as

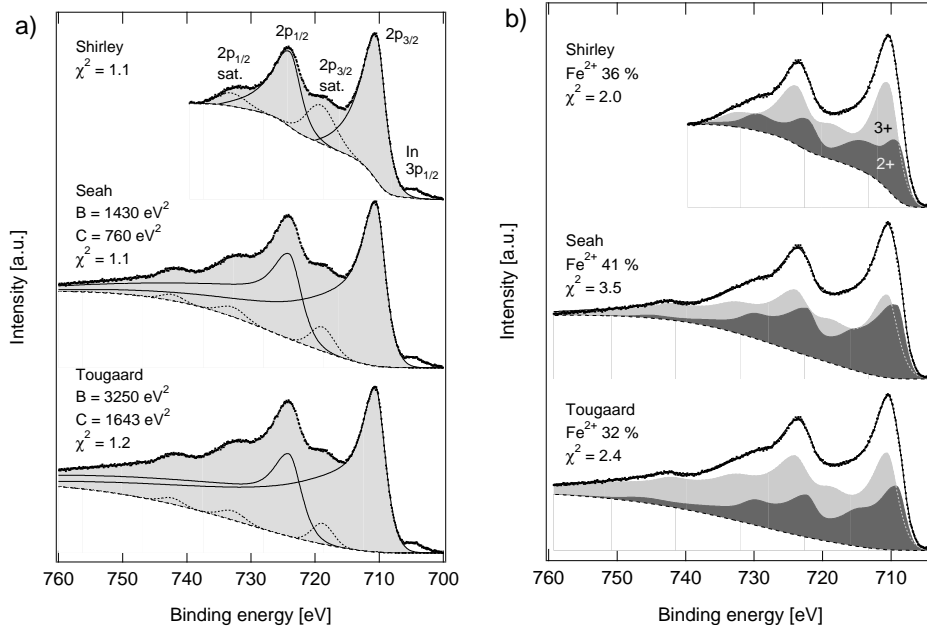$$\chi^2 = \frac{1}{p - n_m}\sum_{i=0}^{p}\left(\frac{F_i - \hat{F}_i}{\sigma_i}\right)^2 \quad (3.11)$$

Figure 3.2: *a) Curve fits to the Fe 2p region of the iron oxide sample (Fe_2O_3) containing only Fe^{3+}; three different background subtraction methods have been applied. The main peaks are drawn with a solid line, the satellites with a dotted line, and the background with a dashed line. The shaded area indicates the sum of the component peaks. b) Decomposition of the Fe 2p region of the analyzed sample (Fe_3O_4) containing Fe^{2+} and Fe^{3+} states. The solid line presents the sum of the two states.*

where p is the number of points, n_m is the number of free fitting parameters, and σ_i is the standard deviation of F_i. Typically, Poissonian counting statistics can be assumed for photoelectrons, i.e. $\sigma_i = \sqrt{F_i}$. It should be noted, however, that although the number of recorded counts follows the Poisson distribution, this is not in general true after the background subtraction which is typically performed before the curve fitting. Thus, when calculating the chi-square, either the background has to be added to the fit to allow the comparison to the recorded data or σ_i has to be estimated in some other way.

Judging by the low chi-square values, the obtained fits in Fig. 3.2 are good. However, the method used for the background subtraction was found to affect the quantification result: for the "Tougaard" background the proportion of the Fe^{2+} state is 32 %, for "Seah" 41 %, and for "Shirley" 36 %.

The choice of the background parameters should be considered carefully. For

Tougaard-type backgrounds, the criterion for the B parameter may be inconvenient if there are interfering peaks in the region where the background should follow the recorded spectrum. For the Shirley background, the choice of the endpoints affects the background shape, and this causes error in particular if the statistical fluctuation in the spectrum is high (low intensity level). By constructing backgrounds with several parameter values, it was observed that for the iron oxide spectrum in Fig. 3.2, having the maximum intensity of about 500 000 counts/eV, this type of error in the Fe^{2+} proportion was less than ± 2 percentage units for all the backgrounds.

Because of the statistical fluctuation (noise) of the counted photoelectrons, a fit to a recorded spectrum, and thereby the proportion of each chemical state, is always subject to random error. The random error of the quantification results can be estimated in two ways: by error propagation or by Monte Carlo simulation. The idea in the *error propagation* approach is to start from the errors in the fitting parameters and estimate their effect on the state area. The covariance matrix V of the fitting parameters m is usually provided by the fitting algorithm. Then, the standard deviation of the area of a given state σ_A can be estimated as

$$\sigma_A \approx \sqrt{\sum_{i,j=1}^{n_\mathrm{m}} \left[\frac{\partial A}{\partial m_i} \frac{\partial A}{\partial m_j} \right]_{m=\mu} V_{ij}} \qquad (3.12)$$

where n_m is the number of the fitting parameters and μ are their fitted values. For most lineshapes, the area cannot be expressed in a closed form and so the derivatives have to be calculated numerically. For the data shown in Fig. 3.2, the standard deviation of the Fe^{2+} proportion was 0.6 percentage units.

When the random error is estimated by the *Monte Carlo simulation*, a set of spectra, typically several hundreds, with an equal noise distribution is first generated, and then the chosen lineshape is fitted to each of the spectra. This produces the distribution of the state area from which the standard deviation can be estimated. In the case presented in Fig. 3.2, a noiseless spectrum was first produced by fitting the lineshape to the data with all parameters free; an alternative way would have been to smooth the recorded spectrum. The random noise was then generated by assuming that for a given data point with N counts, the distribution of noise is Gaussian with a mean of zero and variance of N. After generating 200 spectra with noise, the Fe^{2+} and Fe^{3+} states were fitted to them. The standard deviation of the obtained Fe^{2+} proportions was 0.5 percentage units which is practically equal to that obtained with the error propagation.

In addition to the background subtraction and the random error, the results of the analysis may be affected by systematic errors in the lineshape and model used in the fitting. These errors result when the chosen model would not represent the
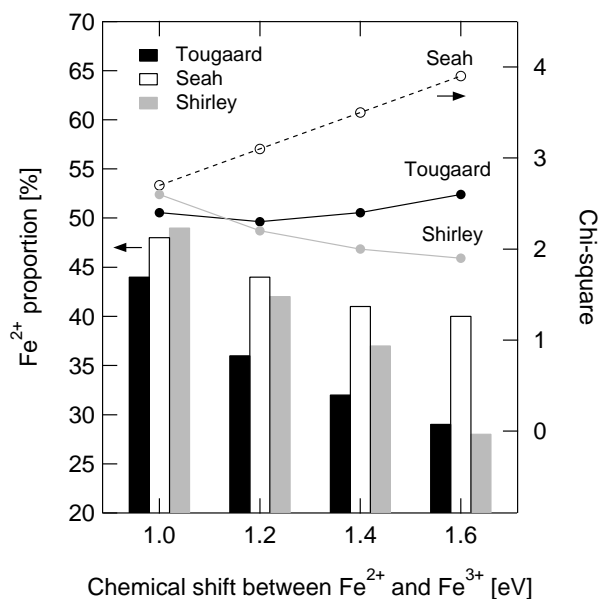
Figure 3.3: *Fe^{2+} proportion as a function of the chemical shift (binding energy separation) between the Fe^{2+} and Fe^{3+} states. The Fe $2p_{3/2}$ binding energy was held at the value obtained from the reference spectrum.*

data even if there were no random error. For example, due to the strong overlap between the Fe^{2+} and Fe^{3+} states, the fitting is sensitive to the assumed binding energy separation, i.e. the chemical shift, between these two states. If several spectra need to be fitted, this parameter has to be fixed in order to obtain consistent results. However, the values reported in the literature range from 1 eV to about 2 eV, see e.g. Refs. [21–23]. Figure 3.3 illustrates the effect of the assumed chemical shift on the proportion of Fe^{2+} for the studied background subtraction methods. It is observed that when the chemical shift increases from 1.0 eV to 1.6 eV, the Fe^{2+} proportion decreases by 15 percentage units for 'Tougaard", 8 percentage units for "Seah", and 21 percentage units for "Shirley". For a given chemical shift value, the background-induced difference in the Fe^{2+} proportion is 5–11 percentage units.

To summarize, uncertainty in the results of XPS curve-fitting originates from (i) the choice of the background subtraction method, (ii) determination of the background parameters, (iii) statistical fluctuation of the recorded intensity, and (iv) systematic errors of the fitting model. The contributions of these error sources in the example case shown in Fig. 3.2 are collected in Table 3.1. It can be concluded that the uncertainty originating from the choice of the background is

Table 3.1: *Estimates for the various sources of uncertainty for the proportion of a given chemical state in Fig. 3.2. The uncertainties are expressed in percentage units.*

background method	± 5
background parameters	± 2
statistical fluctuation	± 1
fitting model	± 5

comparable to other sources of uncertainty. Thus, in order make comparisons between XPS results of, e.g., different authors, the details of the background subtraction and the assumed in-depth distribution need to be taken into account.

3.3 Factor analysis

Factor analysis is a fundamentally different, alternative method to differentiate the contributions of the chemical states in a set of recorded photoelectron spectra. It is a multivariate statistical method which applies to the case where all the spectra of the set can be expressed as linear combinations of a few principal components (factors). The advantages of factor analysis over curve-fitting are that a complete set of spectra can be analyzed at once and that there is no need for a mathematical function describing the lineshape. In addition, factor analysis helps determine the number of chemical states present in the data. The main drawbacks are that factor analysis cannot be used to a single spectrum and that it does not allow shifting or broadening of the spectra.

The objectives of this work are to illustrate the applicability of factor analysis to quantitative determination of chemical states in XPS data, to point out aspects which affect the accuracy of the results, and to propose modifications to the commonly used iterative target transformation factor analysis (ITTFA) technique. The analyzed data consist of simulated model spectra and experimental data on 2p regions of iron and chromium oxides.

Decomposition

In order to apply factor analysis to XPS data, the s measured spectra, each having p points, are first arranged to columns of a data matrix D. The objective of the analysis is to decompose the data matrix D $(p \times s)$ into a product of two

matrices

$$D = RC. \tag{3.13}$$

The columns of R ($p \times n$) are called components or factors and the coefficients for a given component are on the corresponding row of C ($n \times s$) [24]. In terms of XPS this means that each measured spectrum will be expressed as a linear combination of n component spectra, typically corresponding to various chemical states, and the relative amount of each component can be calculated directly from the corresponding column of C.

Decomposition of the data matrix is done by calculating the eigenvectors of the covariance matrix $D^{\mathrm{T}}D$ [24]. A common method for this is singular value decomposition (SVD) which decomposes the data matrix D as

$$D = USV^{\mathrm{T}} \tag{3.14}$$

so that R and C are obtained as

$$R = US \tag{3.15}$$
$$C = V^{\mathrm{T}}. \tag{3.16}$$

Now the columns of R are components that can be used to reproduce the measured spectra, i.e., R forms a basis in which the columns of D can be expressed. Above, S is a diagonal matrix having the square roots of the eigenvalues in decreasing order on the diagonal. The columns of U are the eigenvectors of DD^{T} and the columns of V are the eigenvectors of $D^{\mathrm{T}}D$.

In an ideal case, R would have exactly as many columns as necessary to reproduce D; this is equal to the rank of D. Experimental data, however, contain noise which increases the number of the columns of R equal to the number of the columns of D. It turns out that only the components corresponding to the largest eigenvalues present significant spectral features whereas those with smaller eigenvalues consist mainly of noise. Thus, when determining the number of necessary components, the analyst typically seeks a distinctive drop in the magnitude of the eigenvalues and compares the structure of the components to the noise. In addition, several mathematical functions have been introduced to assist in the determination of the number of necessary components. One of the most commonly used is the indicator function proposed by Malinowski [24].

With the chosen number of components, $\bar{n} < n$, the data matrix is reproduced as

$$D \approx \bar{D} = \bar{R}\bar{C} \tag{3.17}$$

where $\bar{R}$ consists of the $\bar{n}$ first columns of R and $\bar{C}$ of the $\bar{n}$ first rows of C. With a proper number of components, the recorded spectra can be reproduced with decreased noise.

Physical interpretation

Although capable of reproducing the recorded spectra, the columns of $\bar{R}$ are in general not physically meaningful and are thereby called abstract components. In order to obtain a physically meaningful results, $\bar{R}$ and $\bar{C}$ need to be transformed by multiplying them with an appropriate transformation matrix T:

$$X = \bar{R}T \tag{3.18}$$
$$Y = T^{-1}\bar{C}. \tag{3.19}$$

Now the columns of X are the new, physically meaningful components, e.g. the spectra of the different chemical states, and the rows of Y have the corresponding coefficients, i.e. the relative abundances. Mathematically this means that a new basis (columns of X) is formed as a linear combination of the original basis (columns of $\bar{R}$). Because there are infinitely many ways to form the linear combination, the components cannot be determined unambiguously, and the physically meaningful ones are just one combination.

The transformation matrix T can be obtained by guessing the components and expressing them in the basis formed by $\bar{R}$; this method is called target transformation or target testing. It has been shown [24] that for a given test component (vector) $\tilde{x}_l$ a representation, called a predicted component x_l, in the $\bar{R}$ basis is obtained as

$$x_l = \underbrace{\bar{R}(\bar{R}^\mathrm{T}\bar{R})^{-1}\bar{R}^\mathrm{T}}_{\equiv A}\, \tilde{x}_l. \tag{3.20}$$

This transformation minimizes in the least-squares sense the deviation between the test component and the predicted component [24]. It is to be noted that the matrix A is calculated using only the abstract component matrix $\bar{R}$. Thus, each component candidate is transformed independently. Typically, experimental reference spectra or fits to them are used as test components. If $x_l \approx \tilde{x}_l$ within a specified tolerance or the shape of x_l is otherwise satisfactory, x_l is accepted for being used in the final data interpretation. When a necessary number ($\bar{n}$) of linearly independent components have been found, matrix X is formed by setting the vectors x_l, $l = 1\ldots\bar{n}$, as columns. The transformation matrix T is then obtained through Eq. (3.18) as

$$T = \bar{R}^{-1}X. \tag{3.21}$$

Finally, the corresponding coefficients (matrix Y) are calculated with Eq. (3.19).

Component iteration

In reality, a reliable reference spectrum or even a reasonable guess may not be available for the components. In such case an iterative approach can be used: A

simple function, such as a delta peak, is taken as the test initial component and the predicted component calculated using Eq. (3.20). In each iteration round, the predicted component is refined by removing unphysical features and then used as a new test component [25]. Typically, the refining is done by updating points below a certain predetermined intensity level to some positive value. The iteration scheme can be formulated as

$$x_{l,i+1} = A \; x'_{l,i}. \tag{3.22}$$

where $x'_{l,i}$ is the refined version of $x_{l,i}$. The iteration is continued until no refining is needed, i.e. $x'_{l,i} = x_{l,i}$, or if this cannot be achieved in reasonable time, until $x_{l,i+1} \approx x_{l,i}$ within a desired limit. The iteration is done separately for each of the $\bar{n}$ components. This method is called iterative target testing or iterative target transformation factor analysis (ITTFA).

Although knowledge on the peak shape or exact position is not needed in IT-TFA, the analyst has to set values of two parameters for each component: (i) the position of the delta peak serving as the initial test component and (ii) the minimum allowed value (minimum level) for the intensity of the predicted component. When applying ITTFA to XPS data, it was observed that in many cases the values of these parameters cannot be determined unambiguously.

The ambiguity of the minimum level results from the noise. The background subtraction is usually performed so that the mean intensity is about zero in the off-peak region, typically in both ends of the analyzed BE range. In the presence of noise this means that the spectra inevitably contain negative values, and the iteration will typically proceed too long if the minimum allowed intensity value is set strictly to zero. Thus, a negative minimum level is needed but it seems to be impossible to determine any correct value for it. Moreover, the value of the level significantly affects the shape of the predicted component and thereby the analysis results.

Because the delta peak positions and the minimum allowed intensity level cannot be determined a priori, it is convenient to vary these parameters in order to generate different representations for each principal component. With synthetic model data we have observed that if the variation is done with a sufficiently small step size, the set of generated components includes the correct representation for each principal component. In the case of experimental data, there is no general way to identify the correct representation, and thus the practical strategy is to reject the unphysical ones based on the available information on the true shape of the component. Here, at least two requirements for XPS spectra can be used: (i) the component must not have features that go below the noise level and (ii) the chosen set of components must be such that their coefficients (elements of Y) are positive. Depending on the analyzed data, it may be possible to formulate

additional criteria based, e.g., on the symmetry of the peaks. Typically, the analyst ends up with a set of acceptable representations for each component and this determines the uncertainty of the analysis. It should be noted that different representations of the principal components cannot be compared by observing the deviation between the measured and reconstructed data. This deviation only shows how well the data can be expressed with the chosen number ($\bar{n}$) of components and is independent on the shape of the components as long as the components are expressed in the $\bar{R}$ basis.

In this work it was found that if the data can be explained with two components, the component iteration is not needed. It namely turns out that a position can be found where only one multiplication by A (Eq. (3.20)) is enough to transform a delta peak into a physically meaningful component. In practice, the optimal shape for the predicted component can be found by scanning a delta peak through the BE axis using a sufficiently small step size. By using a narrow Gaussian peak as the test component instead of a delta peak, the scanning is not limited by the step size of the recorded data; this usually facilitates finding the optimal component shape.

If three or more components are needed to explain the data, a single multiplication of the test component by A is not always able to generate the correct representation for every principal component, and the iteration is needed to remove the unphysical features. In such case, different representations can be generated by varying both the delta peak position and the minimum allowed intensity level individually for each component.

Examples

Figure 3.4 shows a set of 11 synthetic model spectra generated using two Gaussian peaks with height of 1, FWHM of 2 eV, and centers at 10.0 eV and 11.5 eV. The proportion of the first component, defined here as $A_1/(A_1 + A_2)$ where A_i is the area of component i, increases from 10 % to 90 % through the set. The BE range of the spectra is 20 eV with a step size of 0.1 eV. Gaussian noise with standard deviation of 0.01 was added to the spectra producing a signal-to-noise ratio (SNR) of ~ 95.

Figure 3.5a illustrates the idea of varying the position of the delta peak. At each position, the delta peak is multiplied only once by A (see Eq. (3.20)) and no iteration is performed. The figure clearly indicates that the optimal position for the delta peak can be found around 10.4 eV: setting the delta peak below the optimal position produces components with a negative dip above the peak whereas delta peaks above the optimal position result in asymmetric components with extra intensity on the high BE side. Figure 3.5b shows the optimal predicted
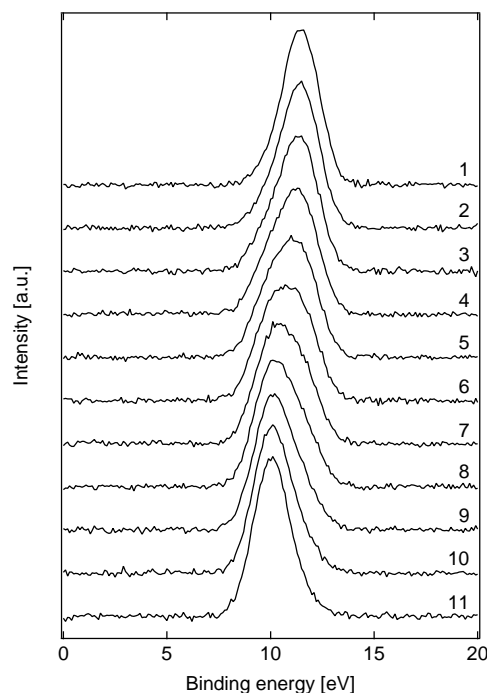
Figure 3.4: *Example of a model data set created using two Gaussian peaks and noise. The component separation is 1.5 eV and the FWHM of the peaks is 2.*

component, searched with a step size of 0.01 eV, for the lower BE component of the model data in Fig. 3.4; also shown is the true component. It is observed that the two spectra are practically identical and the difference is only noise. With a similar procedure the higher BE component can be generated as well. It is to be noted that the delta peak position which produced the optimal shape is not equal to the position of the maximum intensity in the predicted component.

With experimental data the true component shape is not known so the next step after generating a set of predicted components is to reject the unphysical ones. In the example above (Fig. 3.5a), the predicted components with the negative dip can obviously be rejected. On the other hand, the predicted components with extra intensity on the high BE side have no negative features and thus cannot be rejected unless they get negative coefficients (requirement (ii)). If the maximum proportions of the true components in the analyzed set of spectra are less than 100 % (i.e. purely single-component spectra are not included in the set), some non-negative mixed components will always get positive coefficients and have to be accepted. This naturally brings uncertainty to the analysis results which can be reduced only by applying some additional criteria for the component shape.
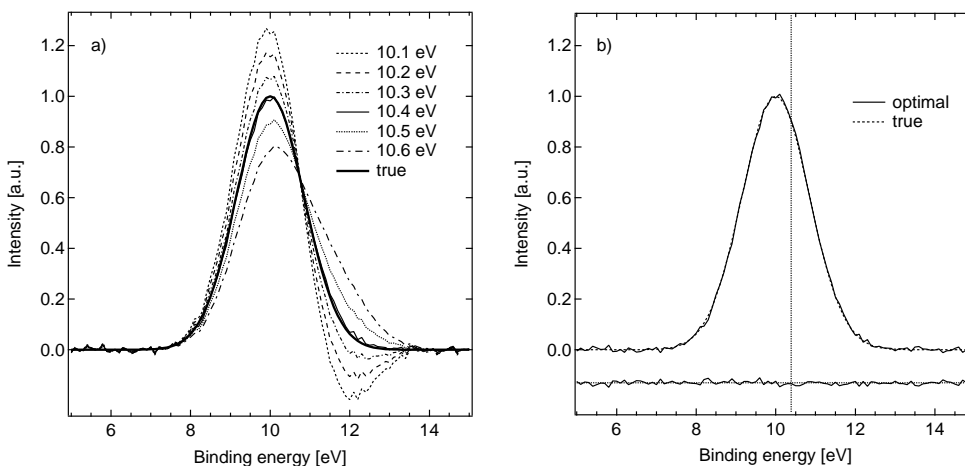
Figure 3.5: *a) Searching the lower BE component of the data in Fig. 3.4: predicted components corresponding to six different delta peak positions with 0.1 eV separation. The true component is shown for comparison. b) Comparison between the optimal predicted component, generated setting a delta peak at 10.39 eV, and the true lower BE component. The difference is shown below the spectra and the optimal delta peak position is indicated with a dotted vertical line.*

In addition to generated model data, factor analysis was also applied to experimental Fe 2p spectra recorded from an iron oxide powder sample sputtered with argon ions. Figure 3.6 shows the spectra and an example of the Tougaard background. The indicator function [24] minimized at 2 suggesting that it is reasonable to represent the data with two components. Using two components is also well justified from the chemical standpoint because oxidized iron is normally encountered in the Fe^{2+} and Fe^{3+} states.

When predicted components were generated by varying the delta peak position with a step size of 0.01 eV, delta peaks around 711.14 eV and 711.70 eV were found to yield spectra that could be interpreted as the Fe^{2+} and Fe^{3+} states, respectively. The $2p_{3/2}$ maximum was at $\sim$ 710.2 eV in the Fe^{2+}-like spectra and at $\sim$ 711.4 eV in the Fe^{3+}-like spectra. These positions as well as the shape of the component spectra agree well with those reported in the literature.

Because the true shape of the component spectra was not known and the variation step size was so small, a group of slightly different predicted components, each with an acceptable shape and no negative features was obtained for both states. Proportions of the Fe^{2+} and Fe^{3+} states were then evaluated corresponding to all possible combinations of these predicted components and only the combinations
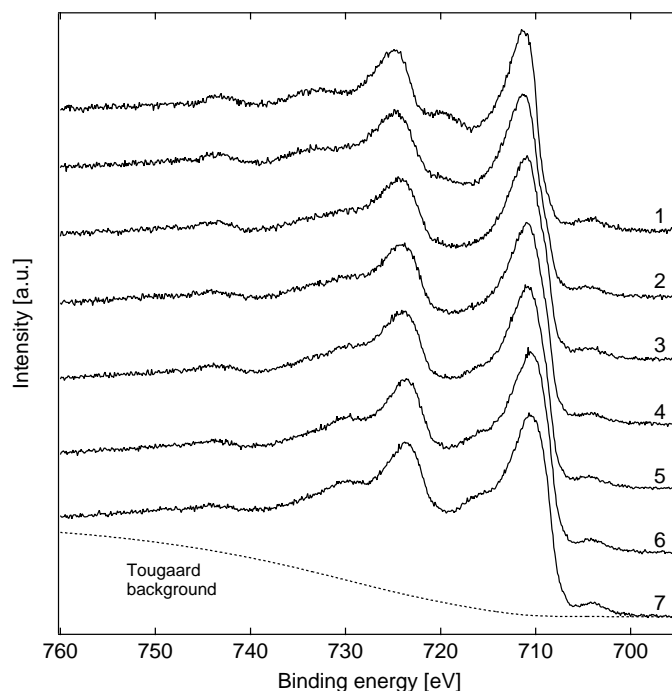
Figure 3.6: *Recorded Fe 2p photoelectron spectra and an example of the used Tougaard background. The cumulative sputtering time increases with the spectrum index. The small peak at ∼ 704 eV comes from the indium foil used as the substrate.*

yielding positive proportions were accepted. Figure 3.7a shows an example of a pair of such accepted components and a reproduction of one of the measured spectra using them. The proportion of the Fe^{2+} state through the analyzed set of spectra is plotted in Fig. 3.7b. The two curves in the figure are the lowest and highest proportions obtained with the accepted components; thus, they represent the uncertainty that results from the lack of reference spectra or other exact knowledge on the component shape. Here, the difference between the lowest and highest Fe^{2+} proportion for a given measured spectrum is about 6 percentage units.

For the sake of comparison, the Fe 2p data was analyzed also with the Shirley background subtracted. Also in this case the data could be explained with two components. The obtained Fe^{2+} proportion in the analyzed spectra deviated 0–20 % units from the results obtained with the Tougaard background (Fig. 3.7b). Thus, the difference in the state proportions caused by the choice of the background subtraction method was in some spectra larger than that resulting
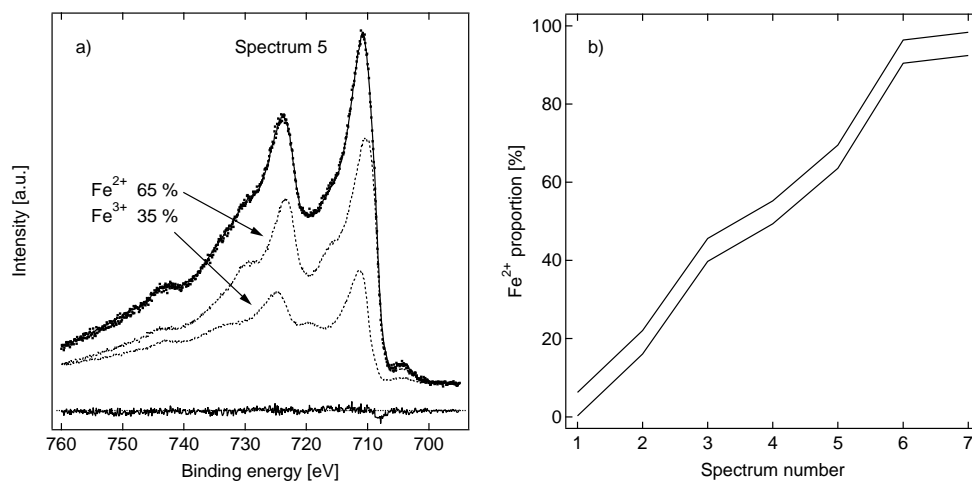
Figure 3.7: *Results of the factor analysis of experimental Fe 2p spectra. a) Spectrum number 5 reproduced using a pair of accepted component spectra. The difference between the measured and reproduced spectrum is shown at the bottom. b) Proportion of the Fe^{2+} state in the analyzed set of spectra. The two lines correspond to the lowest and highest proportions obtained by combining the accepted component spectra.*

from the uncertainty in the component shape. As above, this emphasizes the choice of the background.

Chapter 4

Chromium oxide catalyst

The first application for XPS-based chemical state quantification was a study of chromium oxide catalysts (Publication III). Curve-fitting was chosen as the analysis method instead of factor analysis because the spectra had been recorded with two XPS setups with different settings and, thereby, were not directly comparable.

The amount of information on the catalyst structure and reaction pathways obtainable from catalysts on porous supports is quite limited. Therefore, it is reasonable to construct a model catalyst suited to studies in controlled UHV environment. The insulating nature of common support materials has led to the use of thin oxide films on metals, thus avoiding charging problems. The use of single crystal surfaces with a well-defined oxide structure allows detailed studies of the metal–oxide interface. The most critical requirement for a model catalyst is that it exhibits the same oxidation and reduction properties as the corresponding supported catalysts. This information is most easily obtained with XPS which is sensitive to the chemical state of surface atoms. It has been shown that alumina-supported chromium oxide catalysts have two main oxidation states after calcination in air, Cr^{3+} and Cr^{6+} [26–28]. The activity of the catalyst has generally been assigned to coordinatively unsaturated Cr^{3+} ions. Reduction of the catalysts in, e.g., hydrogen leads mainly to the Cr^{3+} state.

The objective here was to study a $CrO_x/Al_2O_3/NiAl(110)$ model system and compare its behavior to two alumina-supported catalysts, one prepared by impregnation and the other by atomic layer deposition (ALD). The *model catalyst* was prepared by evaporating Cr on a thin alumina film formed on a NiAl(110) single crystal sample. The thin and highly ordered alumina film is considered suitable as a model substrate for catalyst studies, partially owing to its resemblance to the structure of γ-Al_2O_3. The *impregnated catalyst* was prepared from

$Cr(NO_3)_3 \cdot 9H_2O$ on a γ-alumina support. For the *ALD catalyst*, chromium(III) acetylacetonate, $Cr(acac)_3$, was used as the precursor and γ-alumina as the support. After the chemisorption, excess precursor was flushed from the ALD reactor with nitrogen and the acac ligands were removed by air. The preparation procedure consisted of 12 chemisorption–ligand removal cycles.

Information on the chemical state of chromium ions was obtained by analyzing the Cr 2p photoelectron spectra. Reference spectra were recorded for metallic chromium (foil sample) and for the Cr^{3+} state (Cr_2O_3 powder sample), and the parameter values obtained from these fits were used later in the analysis of the catalyst sample. No reference sample was measured for the Cr^{6+} state; instead, the parameters were allowed to vary when fitting the first analyzed spectrum and then fixed to these values for the rest of the spectra. A Shirley background was subtracted form the spectra before the curve-fitting.
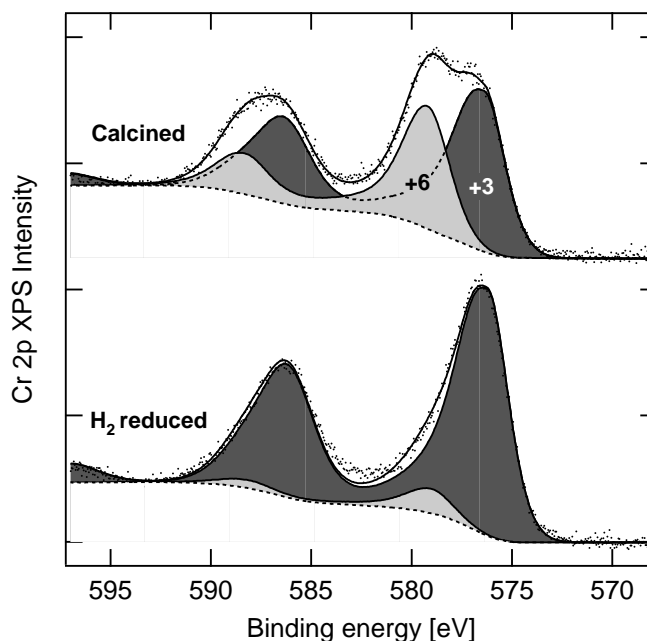

Figure 4.1: *Chemical state analysis of the ALD catalyst sample after calcination in air and after subsequent reduction in hydrogen.*

First, all samples were calcined at 850 K in undried air to achieve an even oxidation state distribution throughout the sample. Then, the samples were reduced in several gases: H_2, CO, CH_4, and n-butane. Figure 4.1 shows two examples of the Cr 2p spectra recorded after treatments. It is observed that after the calcination both Cr^{3+} and Cr^{6+} states are present, whereas mainly Cr^{3+} is found after the

H_2 treatment. Signals that could be attributed to Cr^{2+}, Cr^{4+} or Cr^{5+} could not be identified after any treatments, indicating that their concentration was well below 5 %.

Table 4.1 summarizes the analysis results for the three studied catalyst samples. The impregnated and ALD catalysts are found to behave quite similarly in oxidation and reduction treatments. The slightly higher amount of Cr^{6+} observed in the ALD catalyst after oxidation could be explained with better dispersion reported in literature [27]. The $CrO_x/Al_2O_3/NiAl(110)$ model system was found to behave in a similar way in oxidation and reduction as the alumina-supported catalysts. This indicates that although the structures of the support materials differ greatly, the model system is representative and can be used in further studies. These chromium oxide catalysts have been considered in more detail in Ref. [29].

Table 4.1: *Proportion of Cr^{6+} of all chromium for the studied catalyst samples after calcination and reduction. The estimated error for an individual amount is ± 2 percentage units.*

Catalyst	Calcined [%]	Reduced [%]
ALD	30–41	< 10
Impregnated	20–31	< 10
Model	19	< 5

Chapter 5

Iron oxide thin film for a gas sensor

The second application for XPS-based chemical analysis was a study of an iron oxide thin film serving as a gas-sensitive material. Here, both curve-fitting and factor analysis were utilized.

Semiconductive metal oxides, most commonly SnO_2, TiO_2, and ZnO, are widely studied in order to develop inexpensive and simple gas sensors. Their applications are typically in monitoring combustible or toxic gases, such as O_2, CO, H_2, NO_2, and CH_4. The metal oxide functions as a gas-sensitive material by changing its resistance due to exposure to oxidizing or reducing gases. Typically, the target gas affects the sensor resistance by (i) changing the density of adsorbed oxygen ions generating localized surface states that trap conduction band electrons and/or (ii) changing the concentration of oxygen vacancies acting as donors in an n-type semiconductor [30].

The sensitivity of a given oxide is affected by its chemical and structural properties which, in turn, depend on the characteristics of the preparation procedure. The gas-sensitive material can be incorporated in the sensor as a thick film, thin film, or compressed, and possibly sintered, powder. The advantage of using a thin film, as in this study, is that it makes the sensor fabrication compatible with IC manufacturing processes, thus allowing miniaturization and low production costs. In addition, a thin sensing layer results typically in high sensitivity, rapid response, and low power consumption.

In this work, the chosen film deposition technique was first studied by determining the influence of the deposition parameters on the film characteristics (Publication IV). Then, a sensor sample was constructed and its structural, chemical, electrical, and gas-sensing properties were studied (Publication V). Finally, the relation

between the chemical state of the surface and its oxygen-sensing properties was investigated (Publication VI).

5.1   Growth and characterization

Iron oxide films were grown on a glass substrate with the ALD method using $FeCl_3$ and H_2O as precursors. The deposition temperature was varied between 350 and 500 °C and the number of ALD cycles between 50 and 5000.

The deposition temperature was found to affect the crystal phase and the grain size of the film. The recorded XRD spectra, shown in Fig. 5.1, indicate that the phase changes from γ-Fe_2O_3 to α-Fe_2O_3 between 350 °C and 400 °C. In addition to γ-Fe_2O_3, the film deposited at 350 °C seems to contain a small amount of γ-FeOOH, probably originating from the precursor. The effect of the deposition temperature on the grain size is illustrated by the AFM images in Fig. 5.2.

XPS data confirmed that iron was in the Fe^{3+} state which is in accordance with the structures observed with XRD. However, when the number of ALD cycles was reduced, a part of of iron was found to be in the Fe^{2+} state.
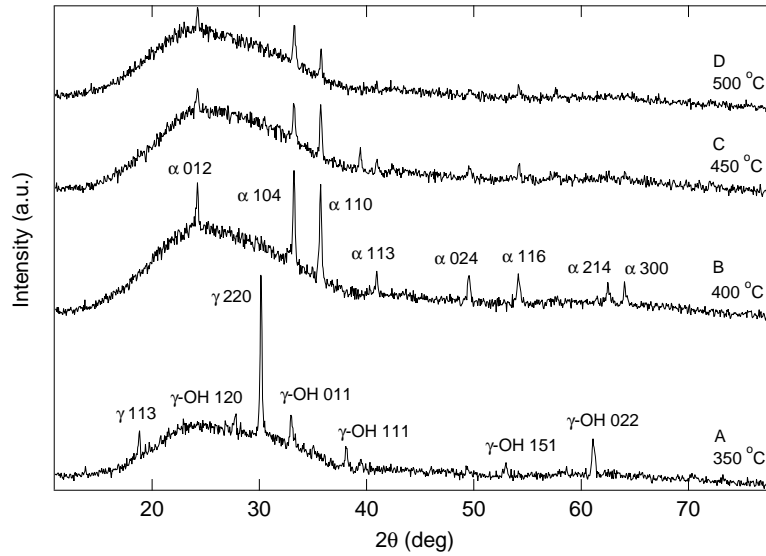

Figure 5.1: *XRD spectra of the iron oxide films grown at 350–500 °C with 5000 cycles. The change from γ-Fe_2O_3 to α-Fe_2O_3 is observed to take place between 350 °C and 400 °C. The sample grown at 350 °C consists of γ-Fe_2O_3 and a small amount of γ-FeOOH. The peaks have been identified according to Ref. [31].*
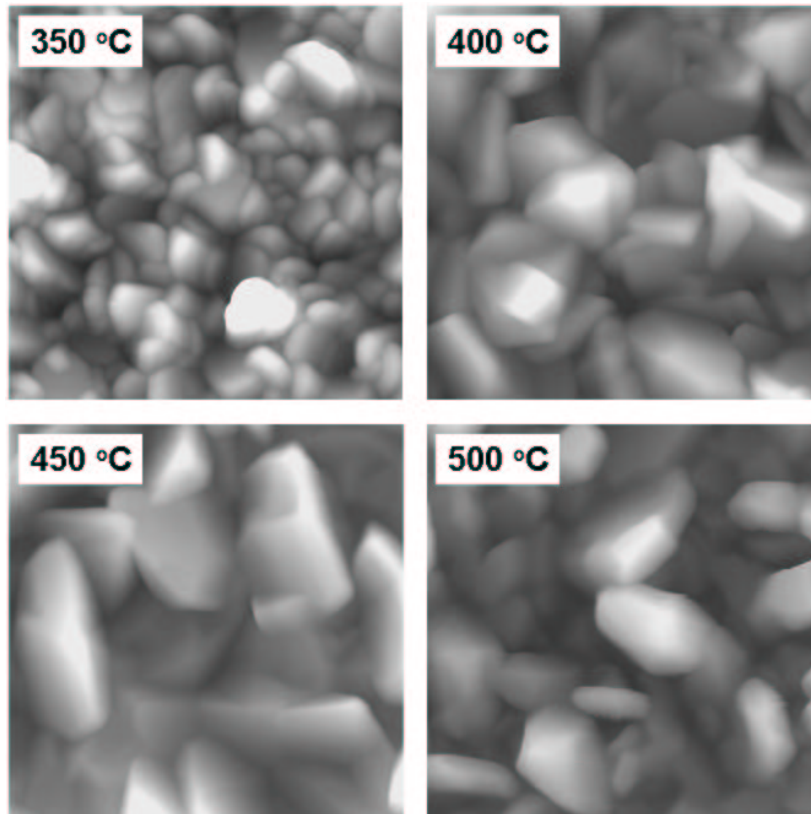
Figure 5.2: *AFM micrographs of the iron oxide films grown at 350–500 °C with 5000 cycles. The size of each image is $1 \times 1 \ \mu m^2$.*

A sensor sample was fabricated using a deposition temperature of 500 °C and conducting 5000 cycles. A high temperature was chosen to ensure thermal stability of the oxide and a high number cycles was used in order to avoid influence of the substrate material and assure a full substrate coverage. Before the film deposition, platinum electrodes for resistance measurement and temperature control were evaporated on the top and bottom side of the glass wafer used as the substrate. After the deposition, the wafer was sawed into 4×4 mm^2 sensor chips which were bonded to TO cases. The results presented here were obtained with an electrode structure, shown in Fig. 5.3, consisting of 22 pairs of interdigital electrodes having a width of 20 μm, length of 0.5–2 mm, and spacing of 20 μm.

Figure 5.4 shows a SEM image of the sensor surface and Fig. 5.5 presents a typical section line measured with AFM. Along with Fig. 5.2 these figures indicate the surface consists of various shapes of agglomerates whose lateral diameter varies
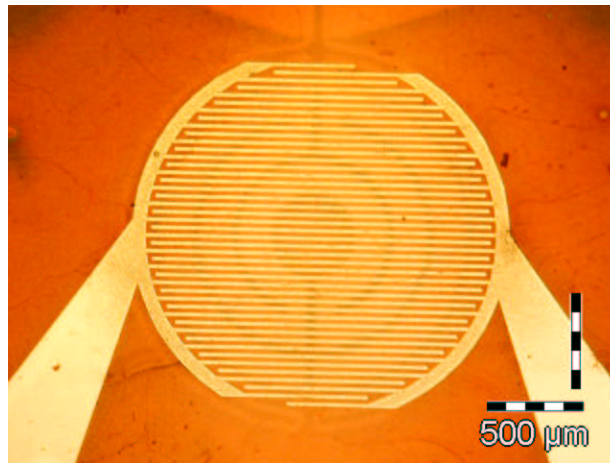
Figure 5.3: *Optical microscope image of the electrode structure for measuring the resistance of the sensor film.*
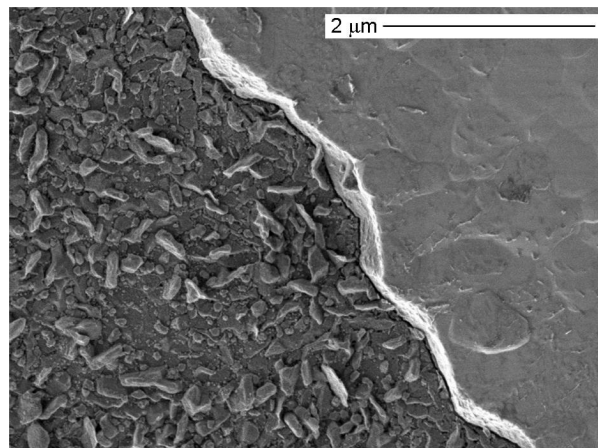

Figure 5.4: *SEM micrograph of the sensor surface. An edge of a platinum electrode is seen on the right.*

typically between 100 and 400 nm and height between 50 and 200 nm. The data indicate also that the film has grown mainly on the glass substrate leaving the platinum electrodes mostly uncovered; only separate grains of iron oxide could be detected on the electrodes. The absence of iron oxide on the electrodes was confirmed with XPS by monitoring the Fe 2p intensity while moving the x-ray spot (150 μm) from the substrate onto the electrode.
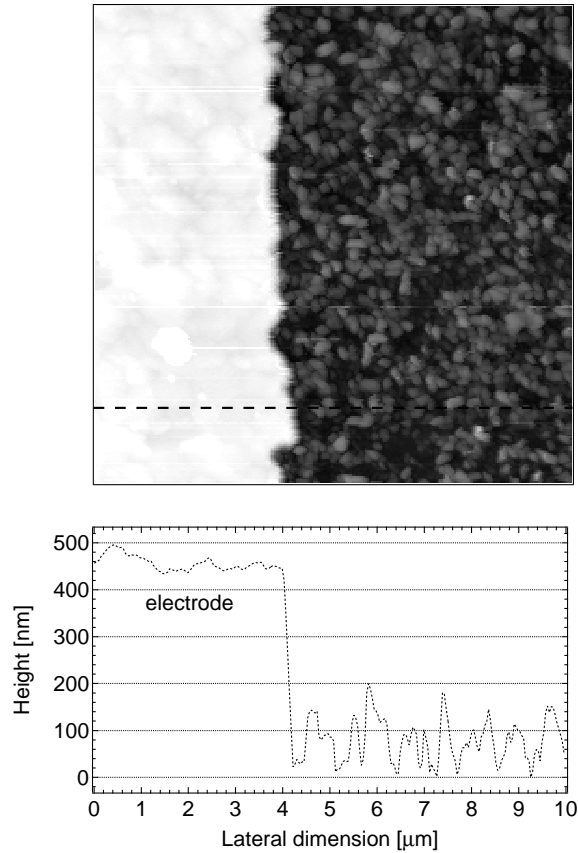
Figure 5.5: *A typical AFM section across the electrode edge (bottom) and the corresponding AFM image ($10 \times 10~\mu m^2$) with the section indicated with a dashed line (top).*

Fe_2O_3 is an n-type semiconductor where the donor states are caused by oxygen vacancies in the lattice [32–34]; the reported band gap values are between 2.0–2.7 eV [35, 36]. The electrical properties of the sensor film were characterized by measuring the Arrhenius curve ($\ln(R)$ vs. $1/T$) and the I–V curve. These were recorded both in a vacuum of 10^{-7} mbar and under oxygen exposure of 10^{-3} mbar. The results are shown in Fig. 5.6. It is observed that the Arrhenius curves are not completely linear in the studied temperature range (100–425 °C) but a straight-line fit gives an activation energy of 0.3–0.5 eV, depending on the points included in the fit. Several sources probably contribute to the activation energy: ionization of donors, hopping of conduction electrons between polaron states, a Schottky barrier at the electrode–semiconductor contact, and a barrier at grain
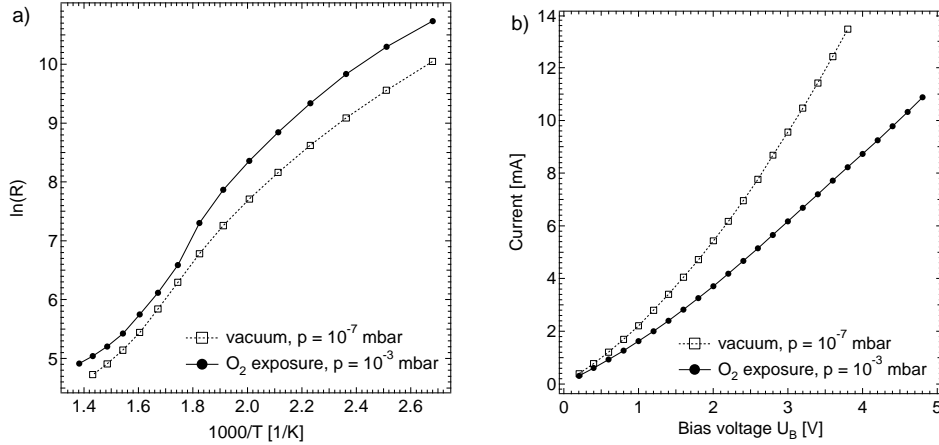
Figure 5.6: *a) Arrhenius curves with $U_B = 2.0$ V and b) I–V curves at 300 °C (right) corresponding to two oxygen pressures. The curves have been drawn to guide the eye.*

boundaries caused by band bending due to localized surface states. However, the Arrhenius plots indicate that although the oxygen exposure decreases the resistance, it does not affect the activation energy. Thus, it seems likely that the sensor response, described below, is not based on changes in the height of the Schottky barrier or the grain boundary barriers. The I–V curves (Fig. 5.6b) show that the sensor behavior is close to Ohmic, especially under the O_2 exposure. The slight upward curvature could be ascribed to, e.g., a Schottky barrier at the electrode contact.

5.2 Gas-sensing properties

Response to O_2 and CO

In order to characterize the general gas-sensing behavior of the film, the chamber was first evacuated to 1×10^{-7} mbar and then the sensor at 300 °C was subjected to a gas exposure sequence consisting of 30-min steps described in Table 5.1. O_2 and CO were used as examples of an oxidizing and reducing target gas, respectively.

The dynamic response, i.e. the sensor resistance as a function of time, is plotted in Fig. 5.7. Due to the strong temperature dependency, the resistance has been normalized with the initial resistance of the sensor in vacuum.

Table 5.1: *Steps of the gas exposure sequence corresponding to Fig. 5.7. Duration of each step was 30 min and the sensor temperature was 300 °C.*

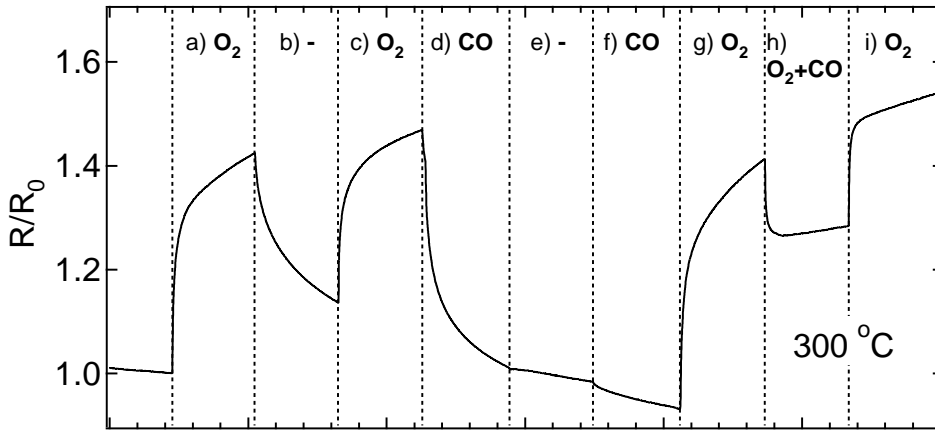| Step	Gas	Pressure (mbar)
initial	vacuum	$\sim 10^{-7}$ mbar
a	O_2	1×10^{-3} mbar
b	vacuum	$\sim 10^{-7}$ mbar
c	O_2	1×10^{-3} mbar
d	CO	1×10^{-3} mbar
e	vacuum	$\sim 10^{-7}$ mbar
f	CO	1×10^{-3} mbar
g	O_2	1×10^{-3} mbar
h	O_2+CO	2×10^{-3} mbar
i	O_2	1×10^{-3} mbar

Figure 5.7: *Dynamic response to successive O_2 and CO exposures at 300 °C. The exposure steps are described in Table 5.1.*

It can be seen that the resistance started to increase rapidly when O_2 was introduced into the chamber (step a), and when the exposure was stopped, the resistance started to decrease (b). According to the commonly used model for the sensing mechanism, see e.g. Ref. [30], the adsorbing oxygen generates localized surface states which trap conduction band electrons; this leads to increase in the resistance. Another possibility is that the adsorbing oxygen enters into

the lattice and fills there oxygen vacancies. This mechanism, too, decreases the density of conduction electrons leading to increase in the resistance. Step b in the dynamic response (Fig. 5.7) shows that when the O_2 exposure was stopped, the surface started to get restored. The effect of CO is observed to depend on the preceding gas exposure: following an O_2 exposure CO made the resistance decrease rapidly (d), whereas after a vacuum period (e) its effect was negligible (f). The O_2 response of the CO-exposed sensor (g) is almost similar to that of an un-exposed sensor (a). This suggests that CO removed the adsorbed oxygen rapidly (d), the surface became clean (e), and CO was not adsorbed on the clean surface (f). These observations indicate that the sensing of CO occurs mainly via a reaction with the adsorbed oxygen.

When CO was added to the O_2 exposure (with an equal pressure), the resistance decreased sharply (h). This decrease was, however, not as large as in the pure CO exposure (d), and the resistance almost stabilized. Finally, stopping the CO exposure caused the sensor to continue the preceding O_2 response (i). The observed behavior seems to reflect two competing reactions: oxygen adsorption and CO removing the adsorbed oxygen.

Effect of the chemical state

After characterizing the general gas-sensing behavior of the iron oxide film, the relation between the chemical state, determined with XPS, and the sensing properties was studied in more detail. For the sake of simplicity, only oxygen was used here as the target gas.

The generic difficulty in the XPS analysis of gas sensors stems from the limited operating pressure of a typical XPS system combined with the high operating temperature of the sensor. In order to mimic the realistic operation conditions, the gas exposures are typically conducted at an elevated temperature at the atmospheric pressure. When the chamber is then evacuated to UHV for the XPS measurement, the surface chemical state may change due to desorption or diffusion, in particular if the sensor is kept at the operating temperature. Consequently, the recorded photoelectron spectra may not be representative for the sensor surface during the actual sensing. In this work, a setup was constructed which allows simultaneous gas exposure, resistance measurement, temperature control, and XPS data acquisition. By performing the gas exposures at the highest operating pressure of the spectrometer (4×10^{-7} mbar), the XPS spectra could be recorded during the exposure, and the observed chemical changes can be directly correlated with the changes in the electrical and sensing properties.

The sensor surface was modified by argon ion sputtering and the changes induced in the chemical state, resistance, and oxygen-sensitivity were investigated. Due

to a higher sputtering yield of oxygen compared to iron, argon ion sputtering is expected to extract oxygen from the oxide which can be detected with XPS. Fe_2O_3 being an n-type semiconductor with oxygen vacancies acting as donors [32–34], such surface modification should cause significant changes to the sensing behavior of the iron oxide film.

The sensor sample was subjected to a sequence of 17 sputtering and oxygen exposure steps. Each step consisted of

- sputtering with 4-keV argon ions

- recording XPS spectra of Fe 2p (700–745 eV), O 1s (525–540 eV), Pt 4f (68–85 eV), and a survey scan (0–1100 eV)

- recording a 50-min resistance response of the sensor to oxygen at 4×10^{-7} mbar

- recording the same XPS spectra under the oxygen exposure

The sensor resistance was monitored continuously but the bias voltage was minimized when recording the spectra in order to avoid broadening of the peaks. The temperature of the sensor was held at 300 °C throughout each step. A few examples of the recorded Fe 2p and O 1s spectra are shown in Fig. 5.8.

For the quantitative analysis of the chemical state of iron, factor analysis was performed for the Fe 2p spectra. Before that, the Tougaard background was subtracted and the spectra were shifted using the O 1s main peak at 530.3 eV as the reference. The indicator function [24] minimized at 3 suggesting that the data contains three components, most likely Fe^0, Fe^{2+}, and Fe^{3+}. However, because the metallic state seemed to be present only in the last step, the analysis was performed with two components. The obtained components as well as the reproduction of one of the recorded spectra are shown in Fig. 5.9a. The agreement between the reproduction and the data is good and the shape of the components is well in accordance with those presented in Figs. 3.2 and 3.7 above as well as those reported in the literature [21,37]. The agreement between the reproduction and the data was practically equally good for all the recorded spectra.

The results of the factor analysis indicate that iron was initially almost completely in the Fe^{3+} state. This is also supported by the XRD results above (Fig. 5.1) which indicate the α-Fe_2O_3 phase containing only Fe^{3+} cations. A small amount of Fe^{2+} was detected which could be attributed to the reducing effect of the platinum electrodes. This was confirmed by recording the Fe 2p region with the x-ray spot far from the electrodes; this produced a pure Fe^{3+} spectrum.
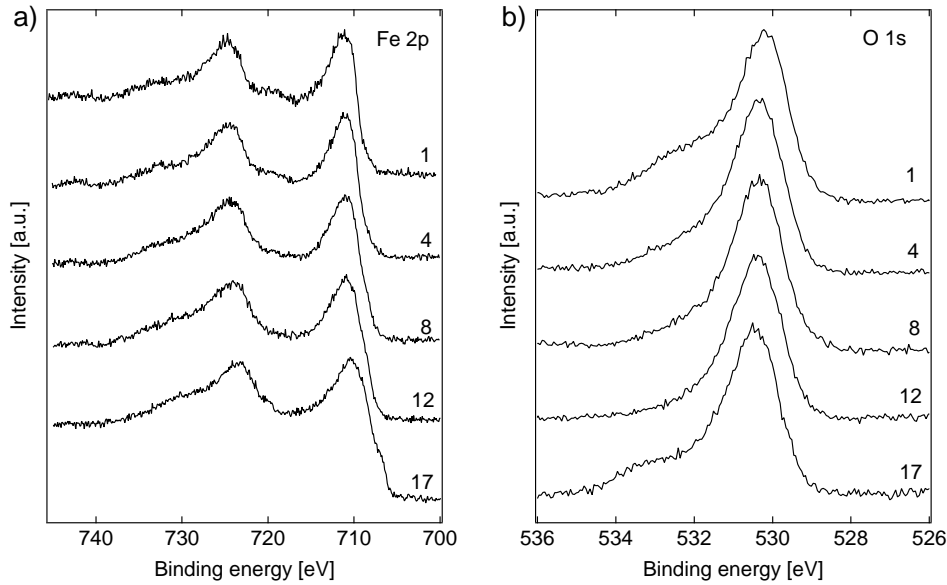
Figure 5.8: *Examples of the recorded Fe 2p (a) and O 1s spectra (b). The index of the step is indicated beside each spectrum, all recorded before the oxygen exposure.*

The broadened shape of the O 1s spectra (Fig. 5.8b) suggests that the oxygen is present in at least two states. Figure 5.9b shows a typical O 1s spectrum fitted with two Gaussian components. The main peak is located at 530.3 eV and has a FWHM of 1.5 eV. Most likely, this corresponds to O^{2-} in the iron oxide lattice. The second component is shifted by about 1.5 eV to higher binding energy and is clearly wider with a FWHM of 2.3 eV. This component could be attributed to OH^- [37–40] originating from H_2O used as the oxygen precursor in the film growth. The high FWHM value suggests that the second peak may also contain an additional unresolved component, such as adsorbed oxygen O^- or O_2^{2-} observed typically at about 0.7 eV and 2 eV higher than the lattice oxygen, respectively [39]. In the last step (Fig. 5.8b, step 17) a new component with a larger separation from the main peak emerged. This could be ascribed to SiO_2 of the substrate.

The results of the factor analysis showed that the argon ion sputtering caused increase in the proportion of the Fe^{2+} state, i.e., reduction of iron. This was probably attributed to the preferential sputtering of oxygen over iron. In the end of the sputtering sequence, iron was practically completely in the Fe^{2+} state and a small amount of metallic iron was detected (Fig. 5.8a, step 17). The O/Fe intensity ratio was observed to decrease corresponding approximately to a change in the stoichiometry from Fe_2O_3 to FeO. This agrees well with the observed
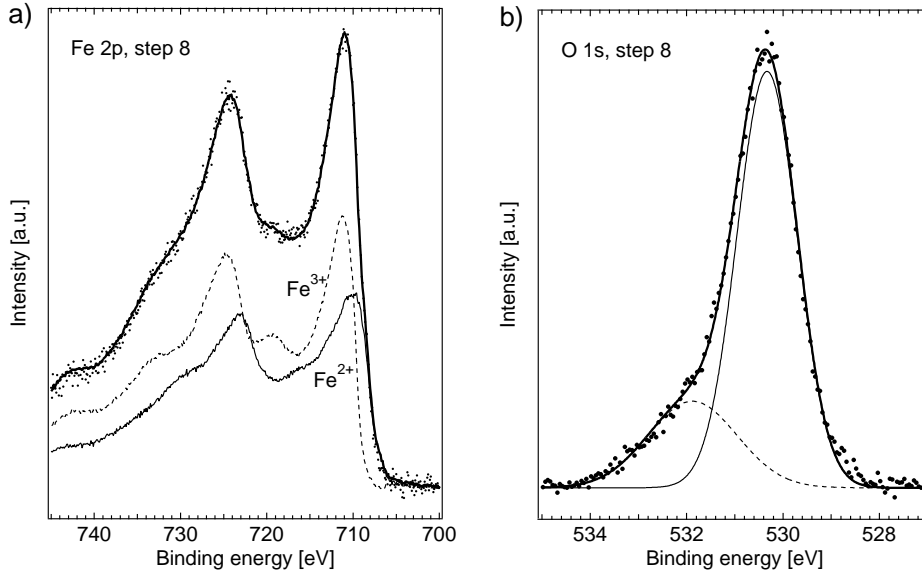
Figure 5.9: *a) Component spectra, Fe^{2+} (solid line) and Fe^{3+} (dashed line), obtained from the factor analysis, and a reproduction (thick solid line) of one of the Fe 2p spectra (step 8). b) One of the O 1s spectra (step 8) fitted with two Gaussian components.*

change in the chemical state of iron: in FeO all iron is in the Fe^{2+} state. Along with the reduction of iron, the sensor resistance decreased over two decades and saturated in the last few steps. This is illustrated in Fig. 5.10. As the iron oxide was initially n-type Fe_2O_3, the decrease in the resistance can be first attributed to generation of oxygen vacancies which act as donors and thereby increase the density of conduction electrons. Another explanation could be change of the conduction mechanism caused by the increase in the amount of Fe^{2+} ions. When the proportion of Fe^{2+} has increased substantially, the conduction behavior can be compared to Fe_3O_4 (33.3 % Fe^{2+}) and FeO (100 % Fe^{2+}) which are oxygen-excess p-type semiconductors having typically very low resistivity compared to Fe_2O_3 [33, 41].

In each step, the oxygen exposure was observed to oxidize iron, increase the O 1s intensity, shift the O 1s spectrum to higher binding energy (band bending), and increase the sensor resistance. The factor analysis results showed that as the sputtering proceeded and the iron became more reduced, the oxidation was enhanced. This was seen as increase in the transfer from the Fe^{2+} to Fe^{3+} state caused by the oxygen exposure. Based on the observation that the oxygen exposure increased the intensity of the O 1s main component, it can be concluded that
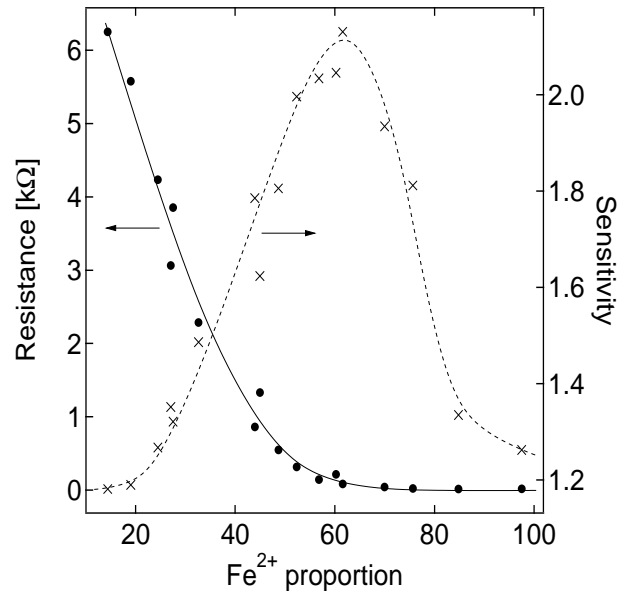
Figure 5.10: *Dependency of the sensor resistance and oxygen-sensitivity at 300 °C on the chemical state of iron. The increase in the Fe^{2+} proportion was generated by argon ion sputtering. The curves have been drawn to guide the eye.*

the gas phase oxygen reacted with the surface and became incorporated into the iron oxide lattice filling there oxygen vacancies. This is consistent with the observed oxidation of iron. The difference between the O 1s spectra recorded before and during the oxygen exposure was about 0.2 eV. This could be interpreted as band bending, as done by Maffeïs et al. [42], although adsorbed oxygen species, which would produce the localized surface states, could not be unambiguously detected with XPS.

The oxygen-sensitivity of the iron oxide film was determined as $R(50)/R(0)$ where $R(0)$ is the sensor resistance before the oxygen exposure and $R(50)$ is the resistance in 50 minutes of exposure, just before starting the XPS data acquisition. Figure 5.10 represents the sensitivity as a function of the Fe^{2+} proportion. It is observed that the sputtering first increased the sensitivity significantly but in the end the sensitivity collapsed back to its initial level. The behavior before the sensitivity drop can be explained with changes in the oxygen vacancy concentration: Sputtering generates vacancies, thereby increasing the amount of conduction electrons and reducing the film resistance. The oxygen sensing takes place by oxygen filling the vacancies. As the sputtering increases the vacancy concentration, the sensitivity increases.

The sensitivity drop could be explained so that some regions of the film adopted p-type behavior. A p-type oxide has an oxygen excess which causes acceptor states to the band gap [30]. Oxygen exposure increases the acceptor concentration which in turn decreases the resistance. Hence, the response is the opposite compared to the n-type conductivity. As mentioned above, the conduction mechanism in those iron oxide phases that contain Fe^{2+} is p-type [33] and their resistivity is significantly lower than those containing only Fe^{3+} [41]. From this point of view it seems likely that by increasing the proportion of the Fe^{2+} state, the sputtering caused regions with p-type conductivity although the n-type behavior still dominated the sensor response. In addition, the shape of the dynamic response was observed to change with the sputtering time, which could also indicate a change in the conduction mechanism. The n–p change in the response and conduction mechanism of an iron oxide gas sensor has also been reported by Gurlo et al. [34], although there the change resulted from an inversion layer on the surface. Considering other possible explanations for the sensitivity drop, the total Fe 2p intensity was not observed to decrease in the course of sputtering. Any change was neither detected in the effect of the oxygen exposure to the O 1s spectrum, i.e. in the intensity increase and band bending. The film structures before and after the sputtering sequence were compared using AFM but no significant changes in the film morphology could be found.

Chapter 6

Summary

In this work, development of methods for XPS data analysis has been considered with the emphasis on background subtraction, curve-fitting, and factor analysis. The objective of the work is to improve quantitative XPS analysis, in particular the quantification of chemical states of transition metal oxides in the case of homogeneous in-depth distribution. The described analysis methods have been utilized in two different applications, catalysts and gas sensors.

Publication I presents a case study of iron and chromium oxides. A lineshape suitable for fitting their core level spectra is described and the differences between three background subtraction methods are illustrated. When investigating typical sources of uncertainty, the choice of the background turns out to be significant.

Publication II describes factor analysis as an alternative method to decompose the overlapping chemical states in a set of XPS spectra. Again, the samples are iron and chromium oxides. The advantages of factor analysis over curve-fitting are that a complete set of spectra can be analyzed at once and that there is no need for a mathematical function describing the lineshape. On the other hand, factor analysis cannot be used to a single spectrum and random variations in the spectra, e.g. shifts or broadening, degrade the results. In the publication, aspects affecting the accuracy of the analysis results are pointed out and modifications to a commonly used analysis procedure are proposed. It is shown that in the case of two-component data, a simple scanning of a delta peak along the binding energy axis is capable of generating acceptable component spectra.

Publication III illustrates the use of XPS in catalyst studies. The objective there is to compare the behavior of a chromium oxide model catalyst to two industrial catalyst samples. XPS is used to analyze the chemical states of chromium in different oxidation and reduction treatments. The results indicate that the model system is representative and can be used in catalyst studies.

Publications IV–VI deal with the ALD growth of an iron oxide thin film and its use as the functional material of a resistive gas sensor. In Publication IV, the effect of the ALD growth parameters on the film properties is considered. It is found that the crystal phase, grain size, and chemical state can be controlled with the deposition temperature and the number of reaction cycles. Publication V describes the characteristics and general gas-sensing properties of the film as incorporated into a sensor. The film is observed to respond to oxygen exposure by increasing its resistance whereas the response to carbon monoxide is the opposite. Finally, the relation between the chemical state of the film surface and the sensing behavior is investigated in Publication VI. It turns out that the sensor resistance and sensitivity to oxygen depend strongly on the chemical state of iron.

Bibliography

[1] K. Siegbahn *et al.*, *ESCA: Atomic, Molecular and Solid State Structure by Means of Electron Spectroscopy* (Almqvist and Wiksells, Uppsala, Sweden, 1967).

[2] The Noble Prize in Physics, `http://nobelprize.org/nobel_prizes/physics/`, [cited April 14th, 2007].

[3] D. A. Shirley, Phys. Rev. B **5**, 4709 (1972).

[4] S. Tougaard, Surf. Interface Anal. **11**, 453 (1988).

[5] S. Tougaard, Solid State Commun. **61**, 547 (1987).

[6] C. Scharfschwerdt *et al.*, J. Electron Spectrosc. Relat. Phen. **60**, 321 (1992).

[7] S. Tougaard, Surf. Sci. **216**, 343 (1989).

[8] S. Tougaard, Surf. Interface Anal. **25**, 137 (1997).

[9] M. P. Seah, I. S. Gilmore, and S. J. Spencer, Surf. Sci. **461**, 1 (2000).

[10] S. Tougaard, Surf. Sci. **464**, 233 (2000).

[11] M. P. Seah, Surf. Sci. **420**, 285 (1999).

[12] J. Végh, J. Electron Spectrosc. Relat. Phen. **151**, 159 (2006).

[13] S. Tougaard and C. Jansson, Surf. Interface Anal. **20**, 1013 (1993).

[14] C. Jansson *et al.*, Surf. Interface Anal. **23**, 484 (1995).

[15] *X-Probe Software Manual ESCA 8.0*, Surface Science Instruments, California, USA, 1986.

[16] J. C. Fuggle and S. F. Alvarado, Phys. Rev. A **22**, 1615 (1980).

[17] P. M. A. Sherwood, in *Practical Surface Analysis, Volume 1, Auger and X-ray Photoelectron Spectroscopy*, 2nd ed., edited by D. Briggs and M. P. Seah (John Wiley & Sons, Inc., New York, USA, 1990), pp. 555–586.

[18] A. E. Bocquet *et al.*, Phys. Rev. B **46**, 3771 (1992).

[19] R. P. Gupta and S. K. Sen, Phys. Rev. B **12**, 15 (1975).

[20] S. Doniach and M. Šunjić, J. Phys. C **3**, 285 (1970).

[21] T. Fujii *et al.*, Phys. Rev. B **59**, 3195 (1999).

[22] P. Graat and M. A. J. Somers, Surf. Interface Anal. **26**, 773 (1998).

[23] C. S. Kuivila, J. B. Butt, and P. C. Stair, Appl. Surf. Sci. **32**, 99 (1988).

[24] E. R. Malinowski, *Factor Analysis in Chemistry*, 2nd ed. (John Wiley & Sons, Inc., New York, USA, 1991).

[25] P. J. Gemperline, J. Chem. Inf. Comput. Sci. **24**, 206 (1984).

[26] F. Cavani *et al.*, J. Catal. **158**, 236 (1996).

[27] A. Kytökivi *et al.*, J. Catal. **162**, 190 (1996).

[28] W. Grünert *et al.*, J. Catal. **100**, 138 (1986).

[29] J. Sainio, Ph.D. thesis, Helsinki University of Technology, 2005.

[30] M. J. Madou and S. R. Morrison, *Chemical Sensing with Solid State Devices* (Academic Press, Inc., San Diego, USA, 1989).

[31] *Mineral Powder Diffraction File, Data Book, Card 13-534*, JCPDS International Centre for Diffraction Data.

[32] R. F. G. Gardner, F. Sweett, and D. W. Tanner, J. Phys. Chem. Solids **24**, 1183 (1963).

[33] K. H. Kim, S. H. Lee, and J. S. Choi, J. Phys. Chem. Solids **46**, 331 (1985).

[34] A. Gurlo *et al.*, Sens. Actuators B **102**, 291 (2004).

[35] S. Mochizuki, Phys. Status Solidi A **41**, 591 (1977).

[36] K. H. Kim, S. H. Lee, and J. S. Choi, J. Phys. Chem. Solids **46**, 331 (1985).

[37] K. Wandelt, Surf. Sci. Rep. **2**, 1 (1982).

[38] G. Gaggiotti *et al.*, Journal of Applied Physics **76**, 4467 (1994).

[39] T. Kawabe *et al.*, Surf. Sci. **448**, 101 (2000).

[40] W. Lü *et al.*, Appl. Surf. Sci. **147**, 39 (1999).

[41] Y. Nakatani and M. Matsuoka, Jpn. J. Appl. Phys. **22**, 233 (1983).

[42] T. G. G. Maffeïs *et al.*, Surf. Sci. **520**, 29 (2002).